

AD-A233 652

2

RADC-TR-89-372
In-House Report
December 1989

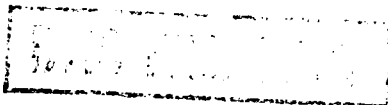


SCANNING IMPEDANCE OF PROXIMITY COUPLED RECTANGULAR MICROSTRIP ANTENNA ARRAYS

Jeffrey S. Herd

DTIC
ELECTE
APR 10 1991
S B D

APPROVED FOR PUBLIC RELEASE DISTRIBUTION UN LIMITED.



Rome Air Development Center
Air Force Systems Command
Griffiss Air Force Base, NY 13441-5700

91 4 09 036

RADC TR-89-372 has been reviewed and is approved for publication.

APPROVED:



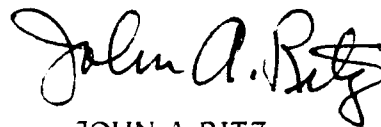
ROBERT J. MAILLOUX
Chief, Antennas and Components Division
Directorate of Electromagnetics

APPROVED:



JOHN K. SCHINDLER
Director of Electromagnetics

FOR THE COMMANDER:



JOHN A. RITZ
Directorate of Plans and Programs

DESTRUCTION NOTICE - For classified documents, follow the procedures in DOD 5200.22-M, Industrial Security Manual, or DOD 5200.1-R, Information Security Program Regulation. For unclassified limited documents, destroy by any method that will prevent disclosure of contents or reconstruction of the document.

If your address has changed or if you wish to be removed from the RADC mailing list, or if the addressee is no longer employed by your organization, please notify RADC (EEAA) Hanscom AFB MA 01731-5000. This will assist us in maintaining a current mailing list.

Do not return copies of this report unless contractual obligations or notices on a specific document requires that it be returned.

REPORT DOCUMENTATION PAGE				Form Approved OMB No. 0704-0188	
1a. REPORT SECURITY CLASSIFICATION Unclassified			1b. RESTRICTIVE MARKINGS		
2a. SECURITY CLASSIFICATION AUTHORITY			3. DISTRIBUTION / AVAILABILITY OF REPORT Approved for Public Release; Distribution Unlimited		
2b. DECLASSIFICATION / DOWNGRADING SCHEDULE					
4. PERFORMING ORGANIZATION REPORT NUMBER(S) RADC-TR-89-372			5. MONITORING ORGANIZATION REPORT NUMBER(S)		
6a. NAME OF PERFORMING ORGANIZATION Rome Air Development Center		6b. OFFICE SYMBOL (If applicable) RADC/EEAA	7a. NAME OF MONITORING ORGANIZATION		
6c. ADDRESS (City, State, and ZIP Code) Hinscom AFB Massachusetts 01731-5000			7b. ADDRESS (City, State, and ZIP Code)		
8a. NAME OF FUNDING / SPONSORING ORGANIZATION		8b. OFFICE SYMBOL (If applicable)	9. PROCUREMENT INSTRUMENT IDENTIFICATION NUMBER		
8c. ADDRESS (City, State, and ZIP Code)			10. SOURCE OF FUNDING NUMBERS		
			PROGRAM ELEMENT NO. 61102F	PROJECT NO. 2305	TASK NO. J3
					WORK UNIT ACCESSION NO. 03
11. TITLE (Include Security Classification) Scanning Impedance of Proximity-Coupled Rectangular Microstrip Antenna Arrays					
12. PERSONAL AUTHOR(S) Herd, J. S.					
13a. TYPE OF REPORT In-House		13b. TIME COVERED FROM _____ TO _____		14. DATE OF REPORT (Year, Month, Day) 1989 December	
				15. PAGE COUNT 64	
16. SUPPLEMENTARY NOTATION					
17. COSATI CODES			18. SUBJECT TERMS (Continue on reverse if necessary and identify by block number)		
FIELD	GROUP	SUB-GROUP			
09	01		Microstrip antennas Phased arrays		
			Proximity coupling Scan blindness		
			Surface waves Scanning impedance		
19. ABSTRACT (Continue on reverse if necessary and identify by block number) Conventional microstrip antenna feeding techniques using microstrip transmission lines or coaxial probes limit the bandwidth to a few percent due to feed radiation and reactive mismatch. Proximity-coupled feeds can be used as an alternative to direct contact feeds on thick substrates by coupling to an embedded microstrip line or by stacking several patches. Proximity-coupled element bandwidths of up to 25 percent have been achieved with single patch elements, but no models presented thus far can predict the effects of inter-element coupling upon resonant frequency and bandwidth. This report presents an infinite array analysis that is applied to three types of proximity-coupled rectangular microstrip elements. The spectral dyadic Green's function for a two layer grounded dielectric slab is used so that all surface wave and mutual coupling effects are included. A method-of-moments with three types of expansion modes is used to efficiently solve for the unknown current distribution, and a model for microstrip traveling wave feed lines in an infinite array is described. Theoretical results are presented for scanning input impedance as a function of substrate parameters, array spacing, and element geometry. Experimental data from a waveguide simulator and an 11 x 11 array are shown to validate the analysis.					
20. DISTRIBUTION/AVAILABILITY OF ABSTRACT <input type="checkbox"/> UNCLASSIFIED/LIMITED <input checked="" type="checkbox"/> SAME AS RPT. <input type="checkbox"/> DTIC USERS			21. ABSTRACT SECURITY CLASSIFICATION Unclassified		
22a. NAME OF RESPONSIBLE INDIVIDUAL Herd, Jeffrey S.			22b. TELEPHONE (Include Area Code) 617-377-4214		22c. OFFICE SYMBOL RADC/EEAA

Preface

The author wishes to acknowledge Dr. Robert Mailloux, Dr. David Pozar, and Dr. Hans Steyskal for helpful discussions of the analysis; Mr. James Kenney for valuable assistance with the experimental measurements, and Mr. Erhard Wisniewski for precise fabrication of the experimental apparatus.

Accession For	
NTIS GRA&I	<input checked="" type="checkbox"/>
DTIC TAB	<input type="checkbox"/>
Unannounced	<input type="checkbox"/>
Justification	
By	
Distribution/	
Availability Codes	
Dist	Avail and/or Special
A-1	

Contents

1. INTRODUCTION	1
2. THEORETICAL ANALYSIS	4
2.1 Integral Equation Formulation	4
2.2 Fourier Transform Green's Function	5
2.3 Moment Method Solution	11
2.4 Expansion and Test Modes	14
2.5 Scanning Impedance Analysis	17
2.6 Mutual Coupling Analysis	24
2.7 Scan Blindness Prediction	27
3. EXPERIMENTAL RESULTS	28
3.1 Waveguide Simulator	28
3.2 11 x 11 Element Array	33
4. BANDWIDTH LIMITATION STUDY	36
5. ARRAY ELEMENT DESIGN STUDY	47
6. CONCLUSIONS	50
REFERENCES	51
APPENDIX: SPECTRAL DYADIC GREEN'S FUNCTION	53

Illustrations

1. Proximity-Coupled Element Geometries	2
2. Delta Function Current Source in a Two-Layer Grounded Dielectric Slab	5
3. Infinite Array of Delta Function Current Sources in a Two-Layer Grounded Dielectric Slab	9
4. Expansion Modes for Proximity-Coupled Element Geometries	12
5. Computed Reflection Coefficient Magnitude of Type A Element as a Function of Scan Angle	20
6. Complex Integration Path Deformation	23
7. Computed Reflection Coefficient Magnitude of Type B Element as a Function of Scan Angle	25
8. Computed Reflection Coefficient Magnitude of Type C Element as a Function of Scan Angle	26
9. Waveguide Simulator	29
10. Measured and Computed Input Impedance of Type A Element in Waveguide Simulator	30
11. Measured and Computed Input Impedance of Type B Element in Waveguide Simulator	31
12. Measured and Computed Input Impedance of Type C Element in Waveguide Simulator	32

Illustrations

13. 11 x 11 Array of Type A Elements	34
14. Measured and Computed Mutual Coupling Coefficients for 11 x 11 Array	35
15. Measured and Computed Scanning Impedance of 11 x 11 Array	37
16. Proximity-Coupled Array Element Bandwidth and Scan Blindness Angle as a Function of Substrate Thickness	38
17. Substrate Combinations for Bandwidth Limitation Study	40
18. Measured and Computed Input Impedance for Case 1A of Bandwidth Limitation Study	41
19. Measured and Computed Input Impedance for Case 1B of Bandwidth Limitation Study	42
20. Measured and Computed Input Impedance for Case 1C of Bandwidth Limitation Study	43
21. Measured and Computed Input Impedance for Case 2A of Bandwidth Limitation Study	44
22. Measured and Computed Input Impedance for Case 2B of Bandwidth Limitation Study	45
23. Measured and Computed Input Impedance for Case 2C of Bandwidth Limitation Study	46
24. Scanning Impedance of Array Element Optimized for Broadside Bandwidth	48
25. Scanning Impedance of Array Element Optimized for Scanning Bandwidth	49

Scanning Impedance of Proximity Coupled Rectangular Microstrip Antenna Arrays

1. INTRODUCTION

Microstrip antenna technology has become versatile and reliable, and features such as low cost, conformality, and reproducibility make the printed circuit antenna an attractive candidate for many antenna array applications. A primary limitation of the conventional microstrip element, however, is an inherently narrow bandwidth. Although this can be improved by increasing the substrate thickness, feed radiation and reactive mismatch make direct-coupled microstrip feed lines or coaxial probes impractical for substrates thicker than approximately 0.05 dielectric wavelengths.

As an alternative, proximity coupling can be used to overcome the substrate thickness limitations imposed by direct-coupled feeds. Figure 1 shows three different microstrip elements that use proximity coupling. Element A consists of two stacked patches; the lower patch is fed by a coaxial probe, and the upper patch is excited by the electromagnetic field of the lower element. Element B also has two stacked patches, with the lower element fed by a coplanar microstrip line. Element C is a single patch that couples electromagnetically to a microstrip line embedded in the dielectric beneath it. These feed

(Received for publication 14 December 1989)

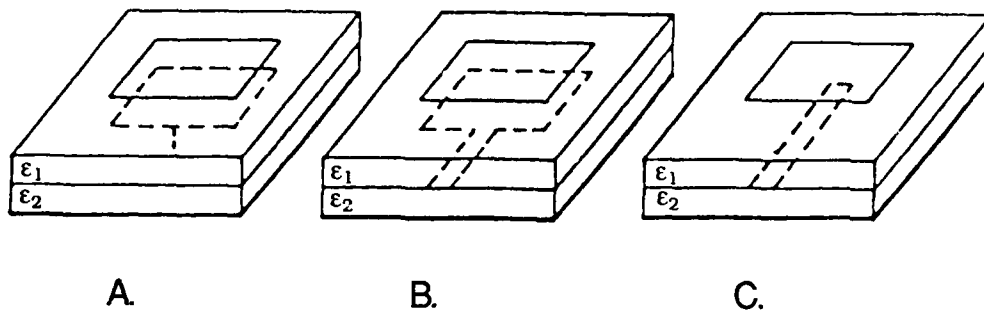


Figure 1. Proximity-Coupled Element Geometries

types make wider bandwidths possible in two ways. First, the overall dielectric thickness can be increased by adding the upper layer without creating additional radiation from the feeds on the lower layer. The additional volume displaced by the element translates into a lower Q , and as a consequence, the bandwidth is increased. Secondly, for elements A and B, wider bandwidths are obtained by offsetting the resonant frequencies of the two patches. Experimental results for isolated proximity-coupled microstrip antenna elements with bandwidths of up to 26 percent have been reported in References.^{1,2,3,4} Although these results indicate a substantial improvement over conventional microstrip antenna bandwidths of 5-10 percent, no studies have been done to assess the effects of mutual coupling and dielectric surface waves in a large array environment.

This report describes a full wave analysis that uses the infinite array spectral

-
1. Yasuo, S., Miyano, N., and Chiba, T. (1983) Expanding the Bandwidth of a Microstrip Antenna, *IEEE AP-S Int. Symp. Digest*, pp 366-369.
 2. Sabban, A. (1983) A New Broadband Stacked Two-Layer Microstrip Antenna, *IEEE AP-S Int. Symp. Digest*, pp. 63-66.
 3. Chen, H., Tulintseff, A., and Sorbello, R. (1984) A Broadband Two-Layer Microstrip Antenna, *IEEE AP-S Int. Symp. Digest*, pp. 251-254.
 4. Cock, R. and Christandoulous, C. (1987) Design of a Two-Layer, Capacitively Coupled, Microstrip Patch Antenna Element for Broadband Applications, *IEEE AP-S Int. Symp. Digest*, pp. 936-939.

dyadic Green's function for electric current sources embedded in a two-layer grounded dielectric slab. This approach has been successfully applied to several printed antenna geometries^{5,6,7} and has the advantage that it includes the effects of surface waves and replicates the mutual coupling environment seen by the elements in a large phased array.

A method of moments is used to solve the electric field integral equation, and three types of expansion modes are used to efficiently model the current distribution on the feed line and patches. A technique is developed for modeling microstrip feed lines in an infinite array unit cell.

Theoretical results are presented for input impedance and scanning bandwidth as functions of substrate parameters, array spacing, element geometries, and feed types. The scan performance of each of the three element types is studied. It is found that scan blindness conditions do occur, and that the blindness angle moves towards broadside with increased dielectric thickness or element spacing. A complete reflection is predicted at the E-plane blindness of element A, and a large, non-unity reflection is predicted for elements B and C. Experimental data from a waveguide simulator and an 11 x 11 array are shown to agree well with the results computed by the model.

The fundamental bandwidth limitations of proximity coupled array elements are investigated, and it is found that the maximum broadside bandwidth that can be attained by the stacked patch element is approximately 25 percent. This limit is shown to be related to the theoretical limit for broadband matching of a complex load impedance, as determined by Fano.⁸

A sample array element is designed for maximum scanning bandwidth, and it is shown that there is a tradeoff between bandwidth and scan range. The sample element is capable of a 10 percent bandwidth (2:1 VSWR) over a 50 degree scan cone.

The computed and measured scanning impedance results indicate that mutual coupling can have a substantial effect upon resonant frequencies and bandwidth in a scanning array environment.

-
5. Pozar, D. and Schaubert, D. (1984) Scan Blindness in Infinite Arrays of Printed Dipoles, *IEEE Trans. Antennas and Prop.*, AP-32:602-610.
 6. Pozar, D. and Schaubert, D. (1984) Analysis of an Infinite Array of Rectangular Microstrip Patches with Idealized Probe Feeds, *IEEE Trans. Antennas and Prop.*, AP-32:1101-1107.
 7. Pozar, D. (1989) Analysis of an Infinite Phased Array of Aperture Coupled Microstrip Patches, *IEEE Trans. Antennas and Prop.*, AP-37:418-425.
 8. Fano, R., (1958) Theoretical Limitations on the Broadband Matching of Arbitrary Impedances, *Journal of the Franklin Institute*, 249:57-84 and 139-154.

2. THEORETICAL ANALYSIS

2.1. Integral Equation Formulation

This work uses the electronic field integration formulation to study the input impedance and radiation properties of proximity-coupled microstrip antenna array elements. To derive the electric field integral equation, we begin with Maxwell's equations for time harmonic fields;

$$\nabla \times \bar{E}(x,y,z) = -j\omega\mu\bar{H}(x,y,z) \quad (1)$$

$$\nabla \times \bar{H}(x,y,z) = j\omega\epsilon\bar{E}(x,y,z) + \bar{J}(x,y,z). \quad (2)$$

An expression for \bar{E} is obtained by taking the curl of Eq. (1) and substituting the curl of \bar{H} on the right-hand side with Eq. (2);

$$\nabla \times \nabla \times \bar{E}(x,y,z) - k^2\bar{E}(x,y,z) = -j\omega\mu\bar{J}(x,y,z) \quad (3)$$

where k is the propagation constant defined as;

$$k^2 = \omega^2\mu\epsilon. \quad (4)$$

Eq. (3) relates the electric field \bar{E} directly to the electric current density \bar{J} .

Next, define a dyadic Green's function to be the solution to a corresponding equation;

$$\nabla \times \nabla \times \bar{G}(x,y,z|x',y',z') - k^2\bar{G}(x,y,z|x',y',z') = -\bar{I} \delta(x-x')\delta(y-y')\delta(z-z') \quad (5)$$

where \bar{I} is the identity dyad and δ is the Dirac delta function. Physically, the Green's function can be interpreted as the electric field of an infinitesimal electric dipole located at $x=x'$, $y=y'$, $z=z'$. In dyadic notation, \bar{G} is defined as;

$$\begin{aligned} \bar{G} = & \hat{x}\hat{x}G_{xx} + \hat{x}\hat{y}G_{xy} + \hat{x}\hat{z}G_{xz} + \hat{y}\hat{x}G_{yx} + \hat{y}\hat{y}G_{yy} + \hat{y}\hat{z}G_{yz} \\ & + \hat{z}\hat{x}G_{zx} + \hat{z}\hat{y}G_{zy} + \hat{z}\hat{z}G_{zz} \end{aligned} \quad (6)$$

where \bar{G}_{ij} represents the \hat{i} -directed electric field of a \hat{j} -directed infinitesimal electric dipole. In general, all nine components of the dyad are required to completely describe the electric field.

The electric field integral equation is obtained by combining Eq. (3) and (5), applying Green's second identity, and choosing appropriate boundary conditions for \bar{G} to get;

$$\bar{E}(x,y,z) = j\omega\mu \iiint \bar{G}(x',y',z') \cdot \bar{J}(x,y,z|x',y',z') dx' dy' dz'. \quad (7)$$

2.2. Fourier Transform Green's Function

The integral equation formulation for the analysis of proximity-coupled microstrip array elements of Figure 1 requires the Green's function for a two-layer grounded dielectric slab. As mentioned earlier, this is identical to solving for the fields of a point source embedded in two layers of dielectric media above a conducting plane, as shown in Figure 2, where \bar{J} is given by;

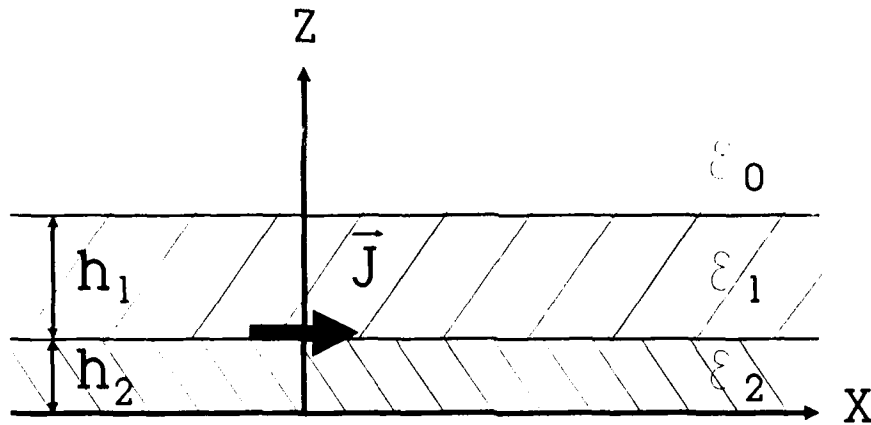


Figure 2. Delta Function Current Source in a Two-Layer Grounded Dielectric Slab

$$\bar{J} = \hat{x} \delta(x-x') \delta(y-y') \delta(z-h_2) \quad (8)$$

The desired fields can be found by working directly with the wave equations for E_z and H_z , and finding the transverse fields from these components.⁹ The wave equations in a source-free region are;

$$\nabla \times \nabla \times \bar{E} - k^2 \bar{E} = 0 \quad (9)$$

$$\nabla \times \nabla \times \bar{H} - k^2 \bar{H} = 0 \quad (10)$$

where $k^2 = \omega^2 \mu \epsilon$, and $\epsilon = \epsilon_2 \epsilon_0$ for $0 < z < h_2$, $\epsilon = \epsilon_1 \epsilon_0$ for $h_2 < z < h_1 + h_2$, and $\epsilon = \epsilon_0$ for $z > h_1 + h_2$.

For the geometry under consideration, the boundary conditions occur at constant z -planes. The Fourier transform method is well suited for solving differential equations with boundary conditions that are unbounded in one or more dimensions. A Fourier transform pair is defined as;

$$E(x,y,z) = \frac{1}{4\pi^2} \int_{-\infty}^{\infty} \int_{-\infty}^{\infty} \tilde{E}(k_x, k_y, z) e^{jk_x x} e^{jk_y y} dk_x dk_y \quad (11)$$

$$\tilde{E}(k_x, k_y, z) = \int_{-\infty}^{\infty} \int_{-\infty}^{\infty} E(x,y,z) e^{-jk_x x} e^{-jk_y y} dx dy. \quad (12)$$

The wave Eqs. (9) and (10) are then Fourier transformed in each region, thereby reducing the problem to one spatial dimension. General solutions for \tilde{E}_z and \tilde{H}_z are therefore;

$$\tilde{E}_z = A e^{-jk'_0 z} \quad z > h_1 + h_2 \quad (13)$$

$$\tilde{H}_z = B e^{-jk'_0 z} \quad z > h_1 + h_2 \quad (14)$$

9. Pozar, D. (1989) Analysis and Design Considerations for Printed Phased Array Antennas, *Microstrip Antenna Handbook*, J. James and P. Hall, Eds., Peter Peregrinus, London.

$$\tilde{E}_z = C e^{-jk'_1 z} + D e^{jk'_1 z} \quad h_2 < z < h_1 + h_2 \quad (15)$$

$$\tilde{H}_z = E e^{-jk'_1 z} + F e^{jk'_1 z} \quad h_2 < z < h_1 + h_2 \quad (16)$$

$$\tilde{E}_z = G e^{-jk'_2 z} + H e^{jk'_2 z} \quad 0 < z < h_2 \quad (17)$$

$$\tilde{H}_z = I e^{-jk'_2 z} + J e^{jk'_2 z} \quad 0 < z < h_2 \quad (18)$$

where

$$k_0'^2 = k_0^2 - \beta^2 \quad (19)$$

$$k_1'^2 = \epsilon_1 k_0^2 - \beta^2 \quad (20)$$

$$k_2'^2 = \epsilon_2 k_0^2 - \beta^2 \quad (21)$$

$$\beta^2 = k_x^2 + k_y^2 \quad (22)$$

In the transform domain, the transverse field components can be expressed in terms of \tilde{E}_z and \tilde{H}_z in each region⁹;

$$\tilde{E}_x = -\frac{jk_x}{\beta^2} \frac{\partial}{\partial z} \tilde{E}_z - \frac{w\mu_0 k_y}{\beta^2} \tilde{H}_z \quad (22)$$

$$\tilde{E}_y = -\frac{jk_y}{\beta^2} \frac{\partial}{\partial z} \tilde{E}_z + \frac{w\mu_0 k_x}{\beta^2} \tilde{H}_z \quad (23)$$

$$\tilde{H}_x = -\frac{jk_x}{\beta^2} \frac{\partial}{\partial z} \tilde{H}_z + \frac{w\epsilon_0 \epsilon_r k_y}{\beta^2} \tilde{E}_z \quad (24)$$

$$\tilde{H}_y = -\frac{jk_y}{\beta^2} \frac{\partial}{\partial z} \tilde{H}_z - \frac{w\epsilon_0 \epsilon_r k_x}{\beta^2} \tilde{E}_z \quad (25)$$

These equations apply to all three regions, with ϵ_r set accordingly to ϵ_2 , ϵ_1 , or 1. The boundary conditions of the problem are;

1. \tilde{E}_x and \tilde{E}_y are zero at $z=0$.
2. \tilde{E}_x and \tilde{E}_y are continuous at $z=h_2$.
3. \tilde{E}_x and \tilde{E}_y are continuous at $z=h_1+h_2$.
4. \tilde{H}_x is continuous at $z=h_2$.
5. $\tilde{H}_y^{(1)}(z=h_2) - \tilde{H}_y^{(2)}(z=h_2) = -e^{-j(k_x x' + k_y y')}$.
6. \tilde{H}_x and \tilde{H}_y are continuous at $z=h_2+h_1$.

Note that a change in the direction of the infinitesimal source or the z -coordinate of the source will require a modification to conditions 4, 5, and 6. Eqs. (12) - (17) for \tilde{E}_z and \tilde{H}_z are substituted into Eqs. (21) - (24), and by applying the boundary conditions above, a set of 10 equations can be solved algebraically for the 10 unknowns. This process is repeated for each of the three source components x , y , and z , so that a complete field dyad is obtained for a source at $z=h_2$. The process is repeated for a source at $z=h_1+h_2$. We shall designate the transformed field dyads as $\bar{Q}(k_x, k_y, z=h_2)$ and $\bar{Q}(k_x, k_y, z=h_1+h_2)$, and they represent a complete description of the transformed fields of arbitrarily oriented infinitesimal dipoles at $z=h_2$ and $z=h_1+h_2$. Algebraic expressions for these \bar{Q} 's are given in the Appendix.

To recover the x and y dependencies, an inverse Fourier transform is taken;

$$\bar{G}(x, y | x', y') = \frac{1}{4\pi^2} \int_{-\infty}^{\infty} \int_{-\infty}^{\infty} \bar{Q}(k_x, k_y) e^{jk_x(x-x')} e^{jk_y(y-y')} dk_x dk_y \quad (26)$$

where $\bar{G}(x, y | x', y')$ is the dyadic Green's function for a source at $x=x'$, $y=y'$.

The spectral dyadic Green's function of Eq. (26) can be generalized to an infinite array of sources.⁵ Figure 3 shows the geometry of an infinite array of horizontal electric dipoles with periodic spacing, a in the x -direction and b in the y -direction. The p, q^{th} source

is located at;

$$x_p = x' + pa \quad (27)$$

$$y_q = y' + qb. \quad (28)$$

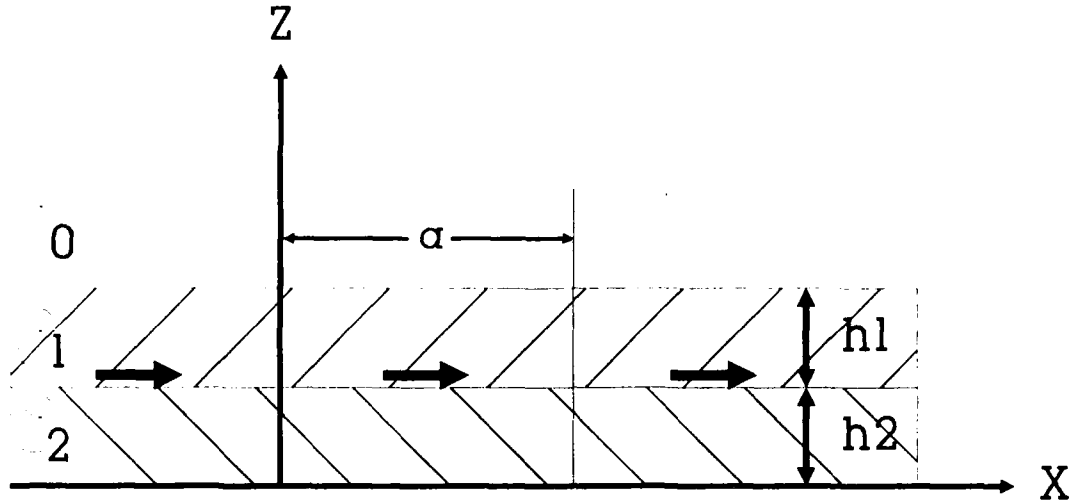


Figure 3. Infinite Array of Delta Function Current Sources in a Two-Layer Grounded Dielectric Slab

In order to scan the array to an angle (θ, ϕ) , the currents on the p, q^{th} source must be phased as;

$$e^{\alpha_{pq}} = e^{-jk_0(pau + qbv)} \quad (29)$$

where

$$u = \sin\theta \cos\phi \quad (30)$$

$$v = \sin\theta \sin\phi \quad (31)$$

The dyadic Green's function of the infinite array is then given by the doubly infinite superposition of fields from each infinitesimal element;

$$\bar{G}_{inf}(x,y | x',y') = \sum_{p=-\infty}^{\infty} \sum_{q=-\infty}^{\infty} e^{-j\alpha_{pq}} \bar{G}_{single}(x-x'-pa, y-y'-qb). \quad (32)$$

Substituting in the expression for \bar{G}_{single} from Eq. (26);

$$\begin{aligned} \bar{G}_{inf}(x,y | x',y') &= \sum_{p=-\infty}^{\infty} \sum_{q=-\infty}^{\infty} e^{-j\alpha_{pq}} \\ &\frac{1}{4\pi^2} \int_{-\infty}^{\infty} \int_{-\infty}^{\infty} \bar{Q}(k_x, k_y) e^{jk_x(x-x'-pau)} e^{jk_y(y-y'-qbv)} dk_x dk_y. \end{aligned} \quad (33)$$

As shown in reference 5, the Poisson sum formula can be applied to Eq. (33) to reduce the doubly infinite summation of doubly infinite integrals to a doubly infinite summation;

$$\bar{G}_{inf}(x,y | x',y') = \frac{1}{ab} \sum_{p=-\infty}^{\infty} \sum_{q=-\infty}^{\infty} \bar{Q}(k_x, k_y) e^{jk_x(x-x')} e^{jk_y(y-y')} \quad (34)$$

where

$$k_x = \frac{2\pi p}{a} + k_0 u \quad (35)$$

$$k_y = \frac{2\pi q}{b} + k_0 v. \quad (36)$$

Eqs. (26) and (34) for the single and infinite array Green's functions can then be used in the integral equation for the field of an arbitrary current distribution as given by Eq. (7) For the single element, Eq. (7) becomes;

$$\begin{aligned} E(x,y,z) &= \frac{j\omega\mu}{4\pi^2} \iiint_{V'} \bar{J}(x',y',z') \\ &\int_{-\infty}^{\infty} \int_{-\infty}^{\infty} \bar{Q}(k_x, k_y, z | z') e^{jk_x(x-x')} e^{jk_y(y-y')} dk_x dk_y dx' dy' dz' \end{aligned} \quad (37)$$

For the infinite array, Eq. (7) can be written as;

$$E(x,y,z) = \frac{j\omega\mu}{ab} \iiint_{V'} \bar{J}(x',y',z').$$

$$\sum_{p=-\infty}^{\infty} \sum_{q=-\infty}^{\infty} \bar{Q}(k_x, k_y) e^{jk_x(x-x')} e^{jk_y(y-y')} dx' dy' dz' \quad (38)$$

with k_x and k_y given by Eqs. (35) and (36). Note that the current distribution \bar{J} in Eq. (38) need only be integrated over the unit cell of the infinite array.

2.3 Moment Method Solution

The unknown electric current density \bar{J} can be solved approximately by applying the moment method procedure to the electric field integral in Eqs. (37) and (38). The boundary condition that the total tangential electric field must equal zero on all conducting surfaces can be written as;

$$E_{\text{tan}} = E_{\text{tan}}^{\text{inc}} + E_{\text{tan}}^{\text{scat}} = 0. \quad (39)$$

Using Eq. (7), this can be rewritten as;

$$- \iint_{S^{\text{inc}}} \bar{J}^{\text{inc}} \cdot \bar{G} ds^{\text{inc}} = \iint_{S^{\text{scat}}} \bar{J}^{\text{scat}} \cdot \bar{G} ds^{\text{scat}} \quad (40)$$

where \bar{J}^{inc} is the incident surface current density, and \bar{J}^{scat} is the unknown scattered current density. As will be discussed later, \bar{J}^{inc} corresponds to the impressed current density on the vertical probe for element A, and is the incident traveling wave current for elements B and C. \bar{J}^{scat} is the surface current density that is induced on the feed line and patches by the fields of the incident current density.

The unknown function \bar{J}^{scat} is then expanded in a set of linearly independent basis functions \bar{J}_n with unknown coefficients I_n ;

$$\bar{J}(x,y,z) = \sum_{n=1}^N I_n \bar{J}_n(x,y,z). \quad (41)$$

The expansion modes are chosen to closely resemble the anticipated current distributions.

Figure 4 shows the three types of modes that are used to analyze the proximity coupled elements, and they will be described in detail in the next section.

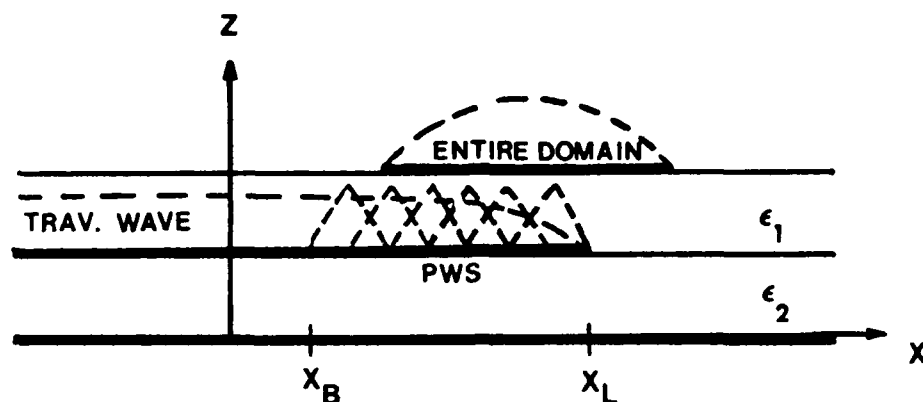


Figure 4. Expansion Modes for Proximity-Coupled Element Geometries

Eq. (41) is then substituted into Eq. (40) and multiplied by a testing function \bar{J}_m , and both sides of Eq. (40) are integrated over the conducting surface of the testing function, s_m ;

$$-\iint_{s_{inc}} \iint_{s_m} \bar{J}_m \cdot \bar{G} \cdot \bar{J}_{inc} ds_m ds_{inc} = \iint_{s_m} \iint_s \bar{J}_m \cdot \bar{G} \cdot \bar{J}_n ds_m ds_n$$

$$m = 1, 2, \dots, N ; n = 1, 2, \dots, N \quad (42)$$

This testing procedure leads to a matrix equation that can be solved for the unknown I_n 's;

$$[Z]^{-1}[V] = [I] \quad (43)$$

where

$$Z_{mn} = \iint_{s_n} \iint_{s_m} \bar{J}_m \cdot \bar{G} \cdot \bar{J}_n ds_m ds_n \quad (44)$$

$$V_m = - \iint_{S_{inc}} \iint_{S_m} \bar{J}_m \cdot \bar{G} \cdot \bar{J}_{inc}^* ds_m ds_{inc}^* . \quad (45)$$

For the single element case, the Green's function of Eq. (26) can be substituted into Eqs. (44) and (45) to get;

$$Z_{mn}^{single} = \iint_{S_n} \iint_{S_m} \bar{J}_m(x,y) \cdot \bar{J}_n(x',y') \\ \cdot \int_{-\infty}^{\infty} \int_{-\infty}^{\infty} \bar{Q}(k_x, k_y) e^{jk_x(x-x')} e^{jk_y(y-y')} dk_x dk_y dx' dy' dx dy \quad (46)$$

and

$$V_m^{single} = - \iint_{S_{inc}} \iint_{S_m} \bar{J}_m(x,y) \cdot \bar{J}_{inc}(x',y') \\ \int_{-\infty}^{\infty} \int_{-\infty}^{\infty} \bar{Q}(k_x, k_y) e^{jk_x(x-x')} e^{jk_y(y-y')} dk_x dk_y dx' dy' dx dy. \quad (47)$$

Next, a Fourier transform of the electric surface current densities can be defined as;

$$\bar{F}_n(k_x, k_y) = \iint_{S_n} \bar{J}_n(x,y) e^{-jk_x x} e^{-jk_y y} dx dy. \quad (48)$$

The exponential factors of the transformed Green's function in Eqs. (46) and (47) can be incorporated with the surface integrals to form Fourier transforms of the electric surface current densities, and the expressions for Z_{mn} and V_m can be rewritten as;

$$Z_{mn}^{single} = \frac{1}{4\pi^2} \int_{-\infty}^{\infty} \int_{-\infty}^{\infty} \bar{F}_m(-k_x, -k_y) \cdot \bar{Q}(k_x, k_y) \cdot \bar{F}_n(k_x, k_y) dk_x dk_y \quad (49)$$

and

$$V_m^{single} = \frac{-1}{4\pi^2} \int_{-\infty}^{\infty} \int_{-\infty}^{\infty} \bar{F}_m(-k_x, -k_y) \cdot \bar{Q}(k_x, k_y) \cdot \bar{F}_{inc}(k_x, k_y) dk_x dk_y. \quad (50)$$

The Fourier transform integrations in Eq. (48) are done in closed form, so the computation of the impedance matrix $[Z]$ and voltage vector $[V]$ is very efficient.

Similarly, when the infinite array Green's function of Eq. (34) is substituted into Eqs. (44) and (45), the expressions for Z_{mn} and V_m can be reduced to;

$$Z_{mn}^{inf} = \frac{1}{ab} \sum_{p=-\infty}^{\infty} \sum_{q=-\infty}^{\infty} \bar{F}_m(k_x, k_y) \cdot \bar{Q}(k_x, k_y) \cdot \bar{F}_n(-k_x, -k_y) \quad (51)$$

and

$$V_m^{inf} = \frac{-1}{ab} \sum_{p=-\infty}^{\infty} \sum_{q=-\infty}^{\infty} \bar{F}_m(k_x, k_y) \cdot \bar{Q}(k_x, k_y) \cdot \bar{F}_{inc}(-k_x, -k_y) \quad (52)$$

with k_x and k_y given by Eqs. (35) and (36).

2.4. Expansion and Test Modes

On the rectangular microstrip patches, entire domain basis functions are used because of their correspondence with the cavity-like behavior of the patches. For \hat{x} -directed currents, the modal functions are given by;

$$\bar{J}_n^{patch}(x, y) = \hat{x} \frac{1}{p_y} \sin \left[\frac{r\pi}{p_x} \left[x - \frac{p_x}{2} \right] \right] \quad (53)$$

where p_x and p_y are the patch dimensions, and r is an integer index accounting for the number of x -variations. The expression for the \hat{y} -directed entire domain current s is given by;

$$\bar{J}_n^{patch}(x, y) = \hat{y} \frac{1}{p_x} \sin \left[\frac{s\pi}{p_y} \left[y - \frac{p_y}{2} \right] \right] \quad (54)$$

where s is an integer accounting for the number of y -variations. Note that the functions in Eqs. (53) and (54) are constant in the \hat{y} and \hat{x} directions, respectively. The Fourier transform of the \hat{x} -directed modes is given by;

$$\bar{F}_n^{patch}(k_x, k_y) = \hat{x} e^{-jk_x(p_x/2)} e^{-jk_y(p_y/2)}$$

$$\left[\frac{\left[\frac{r\pi/p_x}{\left[\frac{r\pi/p_x}{p_x} \right]^2 - k_x^2} \right] \left[e^{jk_x p_x} - \cos(r\pi) \right]}{\left[\frac{r\pi/p_x}{p_x} \right]^2 - k_x^2} \right] \left[\frac{jk_y \left[1 - e^{jk_y p_y} \right]}{k_y^2} \right] \quad (55)$$

For the \hat{y} -directed modes, the Fourier transform is given by;

$$\bar{F}_n^{\text{patch}}(k_x, k_y) = \hat{y} e^{-jk_x(p_x/2)} e^{-jk_y(p_y/2)} \left[\frac{\left[\frac{s\pi/p_y}{\left[\frac{s\pi/p_y}{p_y} \right]^2 - k_y^2} \right] \left[e^{jk_y p_y} - \cos(s\pi) \right]}{\left[\frac{s\pi/p_y}{p_y} \right]^2 - k_y^2} \right] \left[\frac{jk_x \left[1 - e^{jk_x p_x} \right]}{k_x^2} \right] \quad (56)$$

The currents on the microstrip feed lines are modeled by incident and reflected semi-infinite traveling wave modes and sub-domain piecewise sinusoidal modes as in references 10 and 11. The traveling wave modes are the most efficient way to represent the quasi-TEM modes that propagate on a microstrip line, and the piecewise sinusoidal modes model the non-propagating currents excited by the discontinuity in the microstrip lines of elements B and C. Overlapping several piecewise sinusoidal modes on the lower patch of element B helps to enforce continuity of current at the line-patch intersection. More details on the feed modeling will be given in the next section.

The incident currents are given by the expression;

$$\bar{J}_{inc}^{TW}(x, y) = \begin{cases} \hat{x} e^{-jk_e x} & -\infty < x < X_B \\ \hat{x} e^{-jk_e x} \cos\left[\frac{\pi x}{2(X_L - X_B)}\right] & X_B < x < X_L \\ |y| < \frac{W}{2} \end{cases} \quad (57)$$

where k_e is the effective propagation constant of a quasi-TEM mode on the microstrip line. As seen in Figure 4, the traveling wave modes terminate with a one-quarter cycle of a cosine function beginning at $x=X_B$ and ending at $x=X_L$. This feature is helpful in reproducing the shape of the current distribution at the end of the microstrip line, and was found to reduce the number of piecewise sinusoidal modes needed to accurately model the currents there.

The transverse current distribution is assumed to be constant, and this

approximation has been found to be valid in earlier studies.^{10,11} A proportionality constant of $1/W$ is used to normalize the current amplitude, where W is the width of the microstrip line. Using a technique developed in reference 10, k_e is found by using the electric field integral Eq. (7) for the field of an infinite microstrip line, and enforcing the boundary condition that the total tangential electric field is equal to zero across the microstrip line. By applying the Fourier transform method described earlier with a traveling wave mode on the microstrip line, k_e can be computed as the root of the characteristic equation;

$$\int_{-\infty}^{\infty} Q_{xx1}(-k_e, k_y, z=h_1+h_2) F_y^2(k_y) dk_y = 0 \quad (58)$$

where

$$F_y(k_y) = \left[\frac{\sin\left[k_y \frac{W}{2}\right]}{\left[k_y \frac{W}{2}\right]} \right] \quad (59)$$

is the Fourier transform of the transverse current distribution, and Q_{xx1} is given in the Appendix.

The reflected traveling wave currents are given by;

$$\bar{J}_{ref}^{TW}(x,y) = \begin{cases} \hat{x} e^{jk_e x} & -\infty < x < X_B \\ \hat{x} e^{jk_e x} \cos\left[\frac{\pi x}{2(X_L - X_B)}\right] & X_B < x < X_L \\ |y| < \frac{W}{2} \end{cases} \quad (60)$$

The Fourier transform of the incident traveling wave mode is given by;

$$\bar{F}_{inc}^{TW}(k_x, k_y) = \hat{x} F_y(k_y) \left\{ \pi \delta[k_e + k_x] + \frac{j e^{-j(k_e + k_x)X_B}}{[k_e + k_x]} + \right.$$

-
10. Jackson, R. and Pozar, D. (1985) Full-Wave Analysis of Microstrip Open-End and Gap Discontinuities, *IEEE Trans. Microwave Theory and Tech.*, **MTT-33**:1036-1042.
 11. Voda, S. and Pozar, D. (1987) A Rigorous Analysis of a Microstrip Line Fed Patch Antenna, *IEEE Trans. Antennas and Prop.*, **AP-35**:1343-1350.

$$\frac{e^{-j(k_e+k_x)X_L} \left[\frac{\pi}{2(X_L-X_B)} \right] + j(k_e+k_x) e^{-j(k_e+k_x)X_B}}{\left[\frac{\pi}{2(X_L-X_B)} \right]^2 - (k_e+k_x)^2} \quad (61)$$

The Fourier transform of the reflected travelling wave mode is given by;

$$\begin{aligned} \bar{F}_{ref}^{TW}(k_x, k_y) = \hat{x} F_y(k_y) & \left\{ \pi \delta(k_x - k_e) + \frac{j e^{-j(k_x - k_e)X_B}}{(k_x - k_e)} \right. \\ & \left. + \frac{e^{-j(k_x - k_e)X_L} \left[\frac{\pi}{2(X_L - X_B)} \right] + j(k_x - k_e) e^{-j(k_x - k_e)X_B}}{\left[\frac{\pi}{2(X_L - X_B)} \right]^2 - (k_x - k_e)^2} \right\} \end{aligned} \quad (62)$$

The piecewise sinusoidal modes are expressed mathematically as;

$$\bar{J}_n^{PWS}(x, y) = \hat{x} \frac{\sin \left[k_e \frac{L}{2} - |x - x_n| \right]}{w \sin \left[k_e \frac{L}{2} \right]} \quad \begin{aligned} & |x - x_n| < \frac{L}{2} \\ & |y| < \frac{W}{2} \end{aligned} \quad (63)$$

where L is the length of the mode, and x_n is the x -coordinate at the center of the mode. The Fourier transforms of the piecewise sinusoidal modes are given by;

$$\bar{F}_n^{PWS}(k_x, k_y) = \hat{x} \frac{e^{-j k_x x_n}}{\sin \left[k_e \frac{L}{2} \right]} \left[\frac{\cos \left[k_x \frac{L}{2} \right] - \cos \left[k_e \frac{L}{2} \right]}{k_0^2 - k_x^2} \right] F_y(k_y) \quad (64)$$

2.5. Scanning Impedance Analysis

The modeling techniques described in the previous sections can be customized to study each of the three proximity coupled element geometries in Figure 1. The vertical probe feed of element A is modeled by an infinitesimal electric current filament at $x=x_p$, $y=y_p$;

$$\bar{J}_{inc}^{probe}(x, y) = \hat{z} \delta(x - x_p) \delta(y - y_p) \quad (65)$$

The Fourier transform of this function is simply;

$$\bar{F}_{inc}^{probe}(k_x, k_y) = \hat{z} e^{-jk_x x_p} e^{-jk_y y_p} \quad (66)$$

The voltage vector elements are computed by means of the discrete spectral series summations of Eq. (52);

$$V_m^{inf} = \frac{1}{ab} \sum_{i=-\infty}^{\infty} \sum_{j=-\infty}^{\infty} \bar{F}_m(k_x, k_y) \cdot \bar{Q}(k_x, k_y) \cdot \bar{F}_{inc}(-k_x, -k_y) \quad (67)$$

with \bar{F}_{inc} given by Eq. (59), and k_x and k_y given by Eqs. (35) and (36). The impedance matrix elements are computed using Eq. (51);

$$Z_{mn}^{inf} = \frac{1}{ab} \sum_{i=-\infty}^{\infty} \sum_{j=-\infty}^{\infty} \bar{F}_m(k_x, k_y) \cdot \bar{Q}(k_x, k_y) \cdot \bar{F}_n(-k_x, -k_y) \quad (68)$$

The expansion and test modes \bar{F}_{inc} and \bar{F}_n are exclusively entire domain modes given by Eqs. (55) and (56), and \bar{Q} is given in the Appendix. It was found that using the $r=(1,3,5)$ x-directed modes and the $s=(2,4,6)$ modes on each patch gives convergent results for E-plane scan. For off E-plane scans, the $s=(4,6)$ y-directed modes are replaced by $s=(1,3)$ to account for phase asymmetry in the y-direction.

The matrix equation is then solved for the unknown current amplitudes, and the input impedance is calculated by the reaction integral⁶;

$$Z_{in} = \frac{- \int_0^h \bar{J}_{probe} \cdot \bar{E}^{scat} dz}{I_{probe}^2} \quad (69)$$

where \bar{E}^{scat} is the field of the patch currents, and the impressed probe current I_{probe} is chosen to be one ampere. Using Eqs. (7), (34), and (41), Eq. (69) can be rewritten as;

$$Z_m = \frac{1}{ab} \sum_{i=-\infty}^{\infty} \sum_{j=-\infty}^{\infty} \sum_{n=1}^N I_n \bar{F}_m(-k_x, -k_y) \cdot \bar{Q}(k_x, k_y) \cdot \bar{F}_{inc}^{probe}(k_x, k_y). \quad (70)$$

Convergent results were obtained by using 101 terms, $(-50 < i, j < 50)$, in each of the series, and evaluation of the input impedance takes approximately 3 minutes on a DEC MicroVax III.

With the input impedance known, the scanning reflection coefficient can be computed by;

$$R(\theta, \phi) = \frac{Z_{in}(\theta, \phi) - Z_{in}^{\circ}(\theta^{\circ}, \phi^{\circ})}{Z_{in}(\theta, \phi) + Z_{in}^{\circ}(\theta^{\circ}, \phi^{\circ})} \quad (71)$$

when the array is conjugate matched at broadside.

The idealized probe model that was used is identical to the one used in an earlier study.⁶ Although the model ignores the self-reactance of the probe and does not enforce continuity of current at the probe-patch intersection, it has been found that the approximation works well for substrates that are less than 0.05 dielectric wavelengths thick. For larger thicknesses, the self-reactance of the probe and continuity of current must be accurately modeled, and several studies^{12,13,14} have addressed these details carefully.

Figure 5 shows the scanning reflection coefficient for a type A element. There is a total reflection at $\theta=57.9$ degrees in the E-plane, and no blindness in the H-plane. As with an earlier study⁶, it was found that the Green's function for y-directed modes contains a surface wave resonance in the H-plane scan. The resonance causes the Green's function to be singular, and a steady state solution does not exist at that point. The value of the reflection coefficient at that angle is therefore defined to be the value at a vanishingly small offset angle, $R(\theta_{sw} + \Delta\theta)$, where θ_{sw} is the angle of the surface wave resonance.

The microstrip line-coupled elements B and C require all three types of current expansion modes. The electric field integral equation for these elements can be written as:

$$\iint_{s_n} \left[\bar{J}_{inc}^{TW} + R \bar{J}_{ref}^{TW} \right] \cdot \bar{G} ds_M + \sum_{n=1}^{N_{ED+PWS}} I_n \iint_s \bar{J}_n \cdot \bar{G} ds_n = 0 \quad (72)$$

where R is the unknown reflection coefficient, s_M is the surface of the microstrip line, s_n is the surface of the n^{th} expansion mode, and N_{ED+PWS} is the total number of entire domain and piecewise sinusoidal modes. The first integral represents the fields of the incident and reflected traveling wave modes on the microstrip feedline, and the series of integrals represents the fields of the entire domain and piecewise sinusoidal modes.

To replicate the fields of a traveling wave mode on the microstrip feed line in an

-
12. Chew, W. and Kong, J. (1981) Analysis of a Circular Microstrip Disk Antenna with a Thick Dielectric Substrate, *IEEE Trans. Antennas and Prop.*, AP-29:68-76.
 13. Liu, C., Hessel, A., and Shmoys, J. (1985) Performance of Probe-Fed Microstrip-Patch Element Phased Arrays, *Phased Arrays 1985 Symposium Digest*, pp. 157-176.
 14. Aberle, J. and Pozar, D. (1989) Analysis of Infinite Arrays of Probe-Fed Rectangular Microstrip Patches Using a Rigorous Feed Model, *IEE Proceedings*, 136, Pt. H, No. 2.

$h_1 = .159 \text{ cm}$
 $h_2 = .159 \text{ cm}$
 $X_1 = Y_1 = 1.8 \text{ cm}$
 $X_2 = Y_2 = 1.95 \text{ cm}$
 $\epsilon_1 = 2.33 - j.002$
 $\epsilon_2 = 2.33 - j.002$
 $a = 3.35 \text{ cm}$
 $b = 3.60 \text{ cm}$

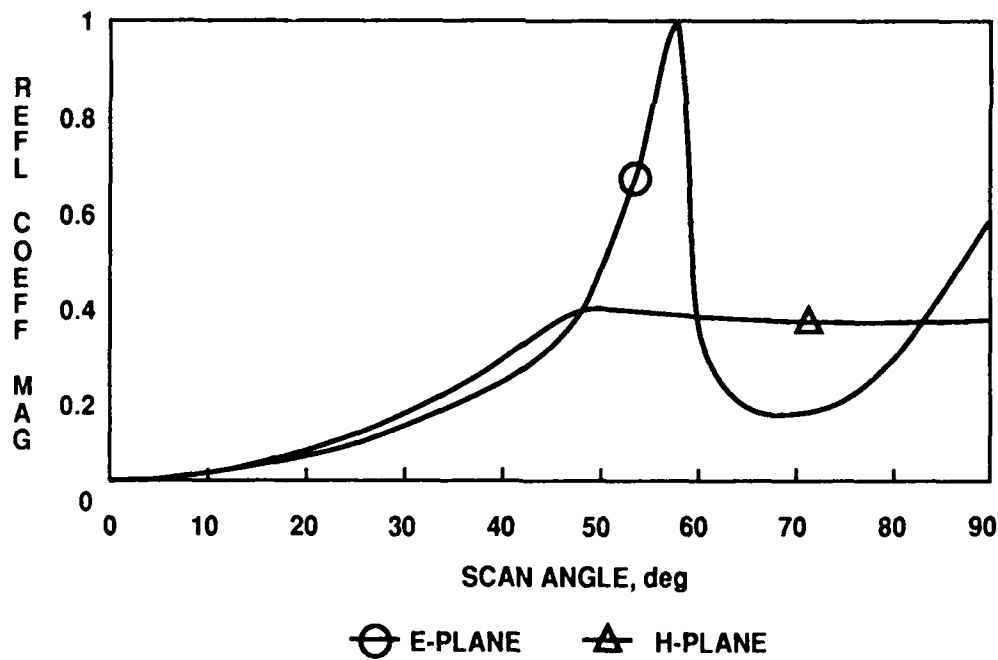
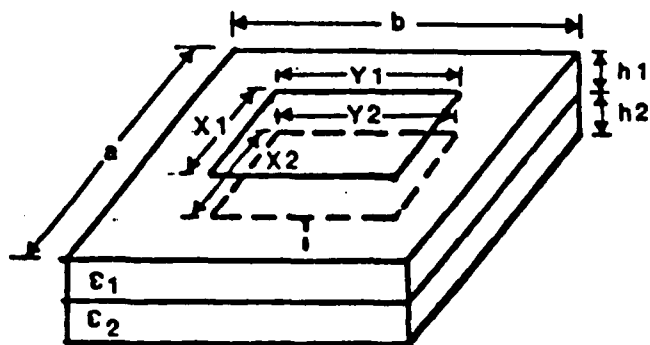


Figure 5. Computed Reflection Coefficient Magnitude of Type A Element as a Function of Scan Angle

infinite array, it was necessary to devise a method of extending the feed lines outside of the unit cell while maintaining the infinite array periodicity. On physical grounds, one can argue that the traveling wave fields are bound closely to the microstrip line, and will, therefore, only excite currents on the unit cell it is feeding. This approximation will be good for microstrip lines that are close to the ground plane, and which do not come in close proximity with other lines or patches. Mathematically, this approximation can be implemented by using the single element Green's function for the traveling wave field integral of Eq. (72), and the infinite array Green's function for the series of integrals representing the fields due to the entire domain and piecewise sinusoidal modes. The infinite array Green's function is used for the piecewise sinusoidal modes because they account for the non-propagating modes excited on the microstrip line, and they radiate fields that are strong enough to excite currents on other elements of the array. The infinite array Green's function must also be used for the entire domain modes because they represent the currents on the microstrip patches, and they couple substantially from element to element. Note that the infinite array Green's function of Eq. (32) reduces to the single element Green's function of Eq. (26) if there is no cell-to-cell coupling.

The moment method procedure described earlier is then applied to Eq. (72) to form a set of linearly independent equations. An additional piecewise sinusoidal test mode provides the extra equation needed to solve for the $N_{ED+PWS}+1$ unknowns. The additional unknown comes from the unknown reflected traveling wave coefficient, R . The matrix equation to be solved for is given by;

$$\begin{bmatrix} Z_{1R} & Z_{12} & \dots & Z_{1N} \\ Z_{2R} & Z_{22} & \dots & Z_{2N} \\ \vdots & \vdots & \ddots & \vdots \\ Z_{NR} & Z_{N2} & \dots & Z_{NN} \end{bmatrix}^{-1} \begin{bmatrix} V_1 \\ V_2 \\ \vdots \\ V_N \end{bmatrix} = \begin{bmatrix} R_1 \\ I_2 \\ \vdots \\ I_N \end{bmatrix} \quad (73)$$

where the subscript R refers to the reflected traveling wave expansion mode.

The expressions for the voltage vector and impedance matrix elements are given by;

$$V_m = \frac{-1}{4\pi^2} \int_{-\infty}^{\infty} \int_{-\infty}^{\infty} \bar{F}_m(-k_x, -k_y) \cdot \bar{Q}(k_x, k_y) \cdot \bar{F}_{inc}^{TW}(k_x, k_y) dk_x dk_y \quad (74)$$

$$Z_{mR} = \frac{1}{4\pi^2} \int_{-\infty}^{\infty} \int_{-\infty}^{\infty} \bar{F}_m(-k_x, -k_y) \cdot \bar{Q}(k_x, k_y) \cdot \bar{F}_{ref}^{TW}(k_x, k_y) dk_x dk_y \quad (75)$$

$$Z_{mn} = \frac{1}{ab} \int_{-\infty}^{\infty} \int_{-\infty}^{\infty} \bar{F}_m(k_x, k_y) \cdot \bar{Q}(k_x, k_y) \cdot \bar{F}_n(-k_x, -k_y) dk_x dk_y \quad (76)$$

(n ≠ R)

where \bar{F}_{inc}^{TW} and \bar{F}_{ref}^{TW} are given by Eqs. (61) and (62), \bar{Q} is given in the Eqs. (88) - (106) in the Appendix, and \bar{F}_m and \bar{F}_n are the piecewise sinusoidal and entire domain expansion and test modes given by Eqs. (55), (56), and (64). As with the probe fed patch, it was found that six entire domain modes on each patch gave convergent results. To improve the modeling of the currents on the microstrip line in the vicinity of the patch, a set of eight piecewise sinusoidal modes are used to compensate for the non-propagating currents near the discontinuities for elements B and C. For element B, the microstrip traveling wave modes and the piecewise sinusoidal modes overlap the patch, and it was found that the results vary only slightly for overlaps between 0.4 and 0.6 times the x-dimension of the patch.

The numerical integrations in Eqs. (74) and (75) are carried out in polar coordinates β and α , defined as;

$$\beta^2 = k_x^2 + k_y^2 \quad (77)$$

$$\alpha = \tan^{-1} \left[\frac{k_y}{k_x} \right]. \quad (78)$$

The limits of integration are $\beta=0$ to ∞ and $\alpha=0$ to 2π . In order to avoid the singularities of the spectral Green's function at the surface wave poles and the traveling wave poles on the real axis, a path deformation technique is used.¹⁵ By introducing an imaginary component of β , the integration path can be deformed sufficiently far away from the real axis to avoid numerical difficulties, as shown in Figure 6. The modified integration path will give the same result as the real axis integration path according to Cauchy's path independence rule, which

15. Newman, E. and Forrai, D. (1987) Scattering from a Microstrip Patch, *IEEE Trans. Antennas and Prop.*, **AP-35**.

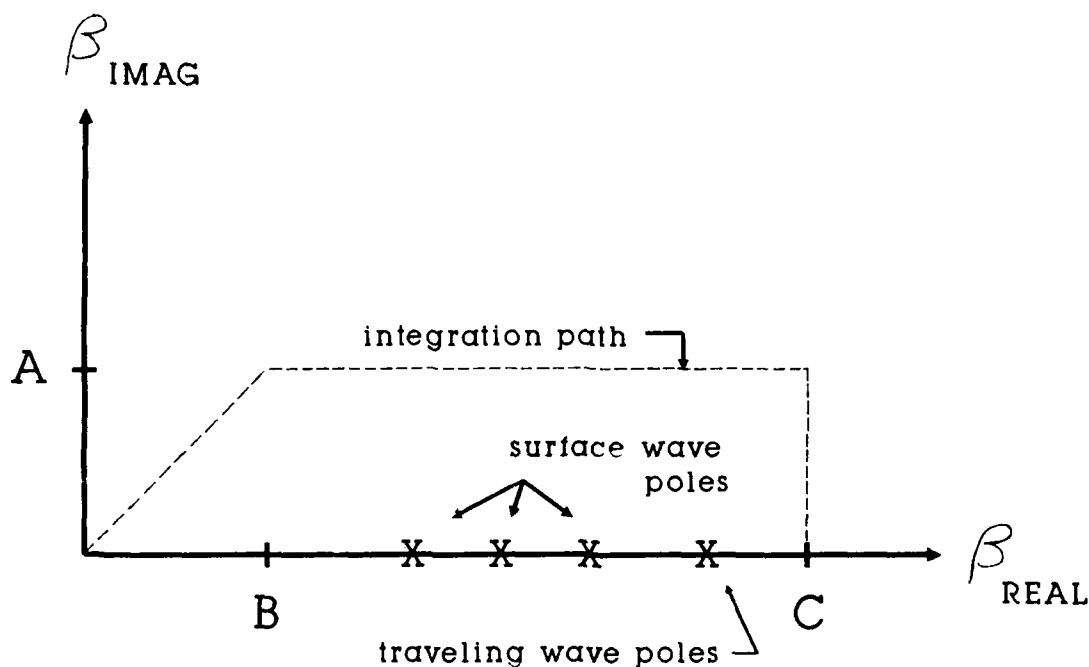


Figure 6. Complex Integration Path Deformation

states that two integration paths in the complex plane give identical results as long as no poles are enclosed by the area between them. Values of $A=0.1k_0$, $B=0.1k_0$, and $C=5.0k_0$ are used, and branch cuts are chosen such that the values of k_z represent outward traveling and decaying waves.

The integration technique was checked by comparing self-and-mutual impedance matrix elements with those from earlier studies on printed dipoles^{16,17}, and the values agreed very closely.

With the reflection coefficient known as a function of scan angle, the scanning impedance can be calculated as;

$$Z_{in}(\theta, \phi) = Z_0 \frac{1 + R(\theta, \phi)}{1 - R(\theta, \phi)} . \quad (79)$$

16. Rana, I. and Alexopoulos, N. (1981) Current Distribution and Input Impedance of Printed Dipoles, *IEEE Trans. Antennas and Prop.*, AP-29:99-105.

17. Alexopoulos, N. and Rana, I. (1981) Mutual Impedance Computation Between Printed Dipoles, *IEEE Trans. Antennas and Prop.*, AP-29(No. 1):106-111.

Using a DEC MicroVax III, computation of the input impedance for a type B element takes approximately ten minutes, and for type C elements it takes approximately eight minutes.

Figure 7 shows the scanning reflection coefficient for a type B element. There is a reflection coefficient magnitude of 0.96 at $\theta=57.9$ degrees in the E-plane, and there is no blind spot in the H-plane. Figure 8 shows the scanning reflection coefficient of a type C element. There is a reflection coefficient magnitude of 0.8 at 47.3 degrees in the E-plane, and no blindness in the H-plane.

2.6. Mutual Coupling Analysis

With the reflection coefficient known as a function of scan angle, it is possible to compute the mutual coupling coefficients between any pair of elements in the infinite array.¹⁸ This is done by expressing the reflection coefficient as a Fourier series expansion;

$$R(u,v) = \sum_{m=-\infty}^{\infty} \sum_{n=-\infty}^{\infty} C_{mn,00} e^{-jmkau} e^{-jnkbv} \quad (80)$$

where

$$C_{mn,00} = \frac{k^2 ab}{4\pi^2} \int_{-\frac{\pi}{ka}}^{\frac{\pi}{ka}} \int_{-\frac{\pi}{kb}}^{\frac{\pi}{kb}} R(u,v) e^{jk(mau+nbv)} du dv \quad (81)$$

is the expression for the mutual coupling coefficient between the center element and the m,n^{th} element, where the element spacings a and b are less than or equal to one half of a wavelength. By symmetry, Eq. (81) can be reduced to;

$$C_{mn,00} = \frac{k^2 ab}{\pi^2} \int_0^{\frac{\pi}{ka}} \int_0^{\frac{\pi}{kb}} R(u,v) \cos(mkau) \cos(nkbv) du dv. \quad (82)$$

Thus, it can be seen that the mutual coupling coefficients of an infinite array can be obtained from the scanning reflection coefficient, $R(u,v)$. As will be seen in the next

18. Hansen, R., (ed.) (1966) *Microwave Scanning Antennas*, Vol.II. *Array Theory and Practice*, Academic Press, New York.

$h_1 = .159 \text{ cm}$
 $h_2 = .159 \text{ cm}$
 $X_1 = Y_1 = 1.87 \text{ cm}$
 $X_2 = Y_2 = 1.96 \text{ cm}$
 $\epsilon_1 = 2.33 - j.002$
 $\epsilon_2 = 2.33 - j.002$
 $a = 3.35 \text{ cm}$
 $b = 3.60 \text{ cm}$
 $W = .40 \text{ cm}$

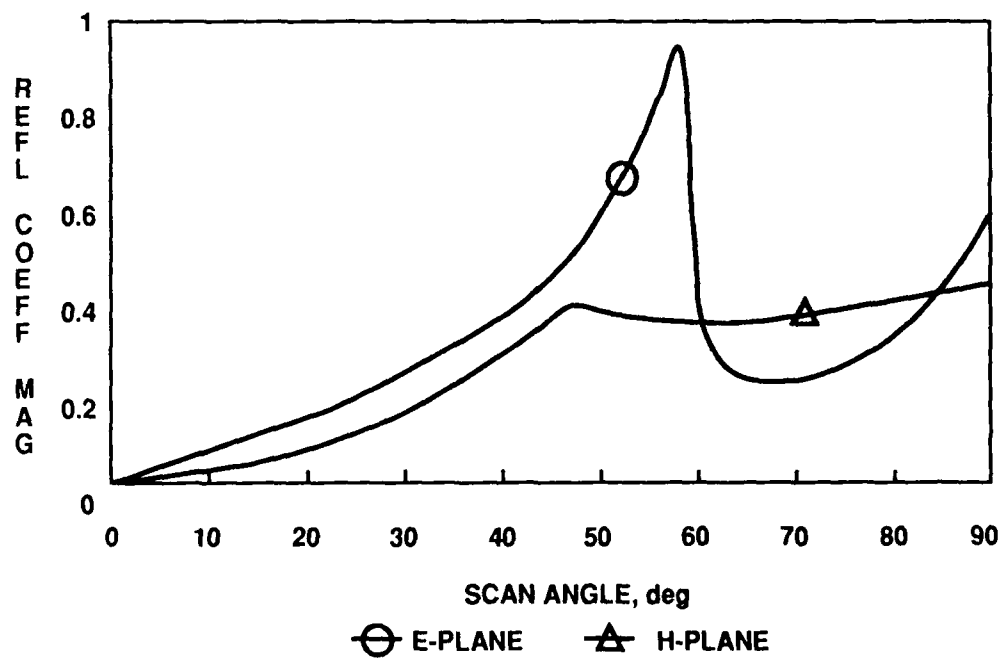
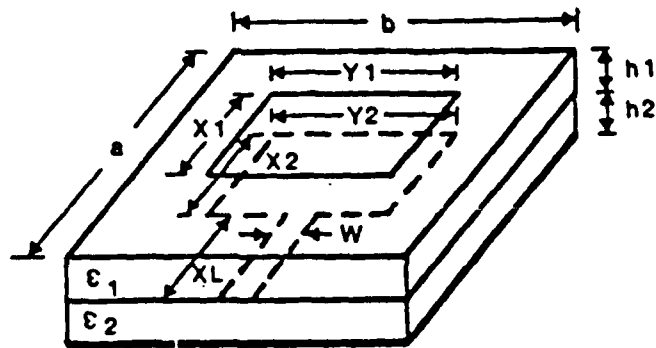


Figure 7. Computed Reflection Coefficient Magnitude of Type B Element as a Function of Scan Angle

$h_1 = .159 \text{ cm}$
 $h_2 = .159 \text{ cm}$
 $X_1 = Y_1 = 1.70 \text{ cm}$
 $X_2 = Y_2 = 0. \text{ cm}$
 $\epsilon_1 = 2.33 - j.002$
 $\epsilon_2 = 2.33 - j.002$
 $a = 3.35 \text{ cm}$
 $b = 3.60 \text{ cm}$
 $W = .40 \text{ cm}$

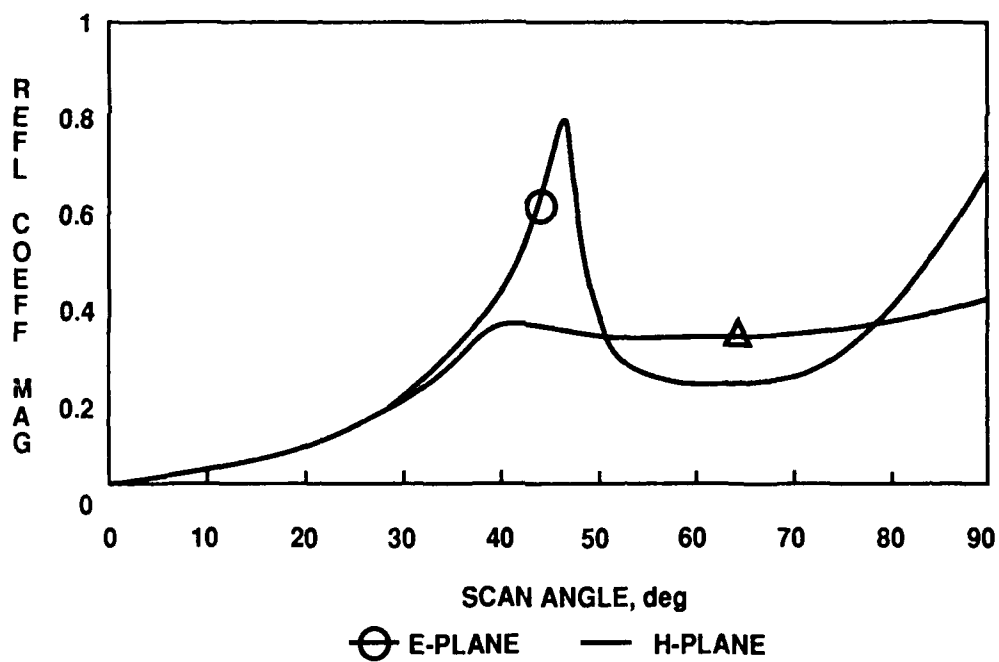
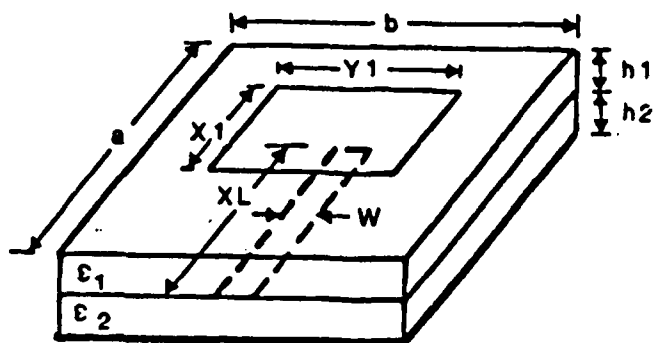


Figure 8. Computed Reflection Coefficient Magnitude of Type C Element as a Function of Scan Angle

section, this method can be used to approximate the scanning reflection coefficient of a finite array by measuring the $C_{mn,00}$ coefficients, and computing $R(u,v)$ from Eq. (80) with a truncated series.

2.7. Scan Blindness Prediction

Scan blindness is a condition where little or no power can be transmitted or received by a phased array for certain scan angles, as indicated by the large reflection coefficient magnitudes in Figures 5, 7, and 8. Equation (80) shows that the reflection coefficient is due to the mismatch of the isolated element plus contributions from all other elements; it is possible for an in-phase accumulation of this coupled power to cause a large reflection at one or more scan angles. This phenomenon has been studied for several infinite microstrip array geometries.^{5,6,7}

When the propagation constant of a surface wave in the loaded dielectric slab matches a Floquet mode propagation constant, it has been found that a forced surface wave will be excited, such that no real power enters or leaves the array surface. Mathematically, this condition can be expressed as⁵;

$$\left[\beta_{sw}\right]^2 = \left[\frac{2\pi m}{a} + k_0 u\right]^2 + \left[\frac{2\pi n}{b} + k_0 v\right]^2. \quad (83)$$

It has also been found⁵ that β_{sw} can be approximated by the surface wave propagation constant of the unloaded dielectric slab over a ground plane. For the two-layer dielectric slab, the TM surface wave propagation constants correspond to zeros of the transcendental equation;

$$\begin{aligned} & \frac{\epsilon_2}{\epsilon_1} k_1' \cos k_2' h_2 \left[\epsilon_1 k_0' \cos k_1' h_1 + j k_1' \sin k_1' h_1 \right] \\ & + j k_2' \sin k_2' h_2 \left[k_1' \cos k_1' h_1 + j \epsilon_2 k_0' \sin k_1' h_1 \right] = 0 \end{aligned} \quad (84)$$

where k_0' , k_1' , and k_2' are defined by Eqs. (19), (20), and (21). The TE surface wave propagation constants are given by the zeros of the equation;

$$\begin{aligned} & k_2' \cos k_2' h_2 \left[k_1' \cos k_1' h_1 + j k_0' \sin k_1' h_1 \right] + \\ & j k_1' \sin k_2' h_2 \left[k_0' \cos k_1' h_1 + j k_1' \sin k_1' h_1 \right] = 0. \end{aligned} \quad (85)$$

It can be seen that these expressions appear in the denominator of the two-layer grounded dielectric slab Green's functions given in the Appendix.

An earlier study¹³ points out that leaky wave blindnesses are also possible in printed circuit arrays, and are particularly noticeable when the patches are operating at frequencies away from resonance. The leaky wave blindness angles can be predicted using an approximation similar to Eq. (83) with β_{sw} replaced by β_{lw} , the propagation constant of a leaky wave in the unloaded dielectric slab. The values of β_{lw} can be computed from the complex zeros of Eqs. (84) and (85), with both real and imaginary parts of the solution greater than zero. Note that the Green's function used in the full analysis of the previous sections will account for all surface waves and leaky waves in the dielectric.

The blindspot angles predicted by Eq. (83) were within one-tenth of a degree of those computed by the full wave analysis in Figures 5, 7, and 8.

3. EXPERIMENTAL RESULTS

3.1. Waveguide Simulator

To validate the theory, a rectangular waveguide simulator was constructed using the S-band waveguide shown in Figure 9. The lowest order TE_{10} mode in the waveguide replicates the fields seen by an element in an infinite periodic array radiating a plane wave in the H-plane at an angle¹⁸;

$$\theta = \sin^{-1} \left[\frac{\lambda}{4b} \right] \quad (86)$$

where $2b$ is the major dimension of the waveguide. The waveguide is terminated in a matched load to prevent reflections back towards the radiating element.

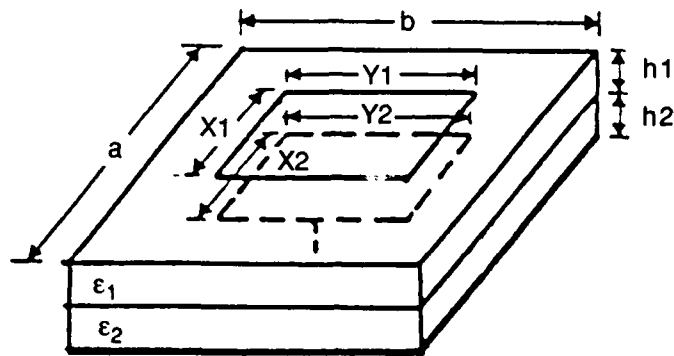
A basic requirement of the waveguide simulator is that the element must have symmetry about its center on the x and y axes. Each of the three element types tested have some form of asymmetry. As can be seen in Figure 1, element A has a probe that is not symmetrical about the center of the x -axis, and elements B and C have microstrip feed lines on one side, also violating the x -axis symmetry. However, these features radiate very little in comparison with the microstrip patches and, therefore, will not substantially excite any waveguide modes that would cause errors in the simulation.

All simulator measurements were made on a calibrated Hewlett Packard 8510 network analyzer. Element A was fed by an SMA coaxial probe connector, with the phase reference at the ground plane. The microstrip lines of elements B and C were fed by a coax-to-microstrip transition through the waveguide wall, with the phase reference at the transition.

Figures 10 - 12 show the simulator measurements and computed data for the three infinite array element types. Excellent agreement was obtained between theory and experiment



Figure 9. Waveguide Simulator



● Measured ▲ Predicted

$h_1 = .159 \text{ cm}$
 $h_2 = .159 \text{ cm}$
 $X_1 = Y_1 = 1.8 \text{ cm}$
 $X_2 = Y_2 = 1.95 \text{ cm}$
 $\epsilon_1 = 2.33 - j.002$
 $\epsilon_2 = 2.33 - j.002$
 $a = 3.35 \text{ cm}$
 $b = 3.60 \text{ cm}$

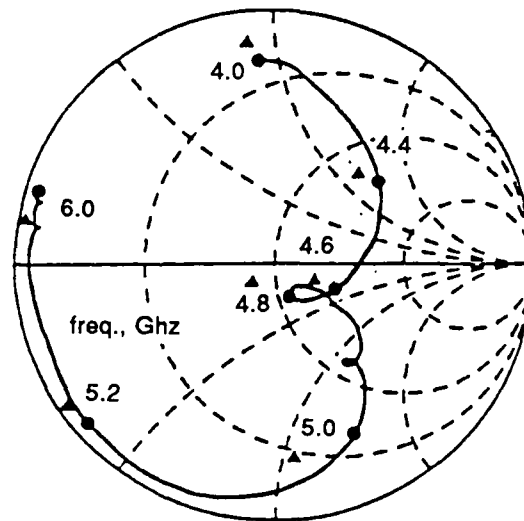
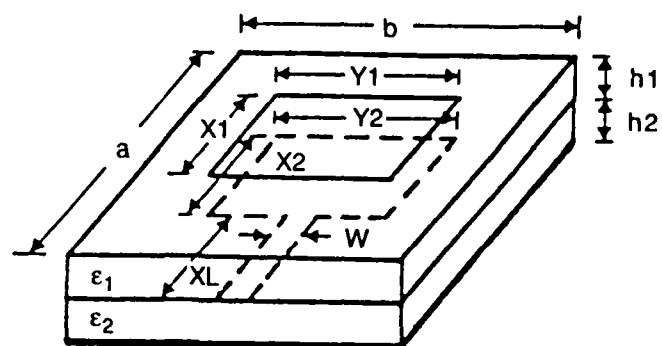


Figure 10. Measured and Computed Input Impedance of Type A Element in Waveguide Simulator



● Measured ▲ Predicted

$h_1 = .159 \text{ cm}$
 $h_2 = .159 \text{ cm}$
 $X_1 = Y_1 = 1.87 \text{ cm}$
 $X_2 = Y_2 = 1.96 \text{ cm}$
 $\epsilon_1 = 2.33 - j.002$
 $\epsilon_2 = 2.33 - j.002$
 $a = 3.35 \text{ cm}$
 $b = 3.60 \text{ cm}$
 $W = .40 \text{ cm}$

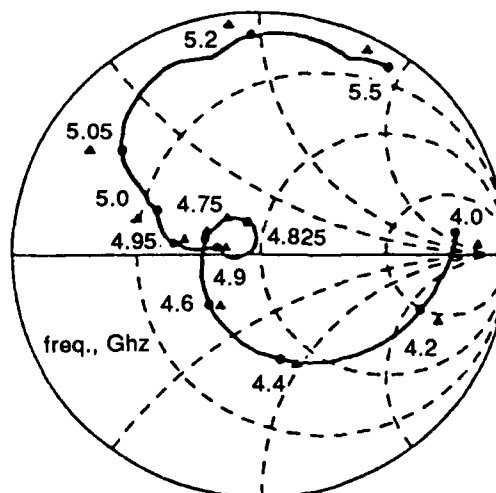
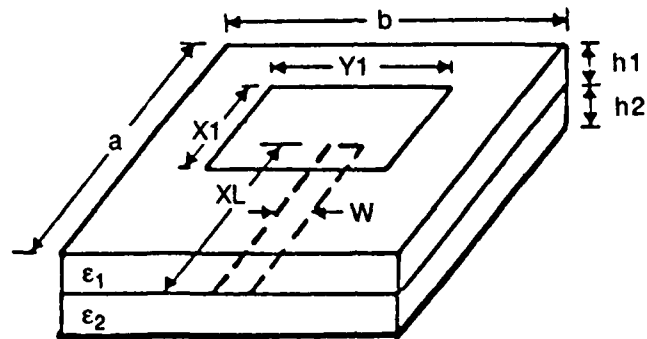


Figure 11. Measured and Computed Input Impedance of Type B Element in Waveguide Simulator



● Measured ▲ Predicted

$h_1 = .159 \text{ cm}$
 $h_2 = .159 \text{ cm}$
 $X_1 = Y_1 = 1.70 \text{ cm}$
 $X_2 = Y_2 = 0. \text{ cm}$
 $\epsilon_1 = 2.33 - j.002$
 $\epsilon_2 = 2.33 - j.002$
 $a = 3.35 \text{ cm}$
 $b = 3.60 \text{ cm}$
 $W = .40 \text{ cm}$

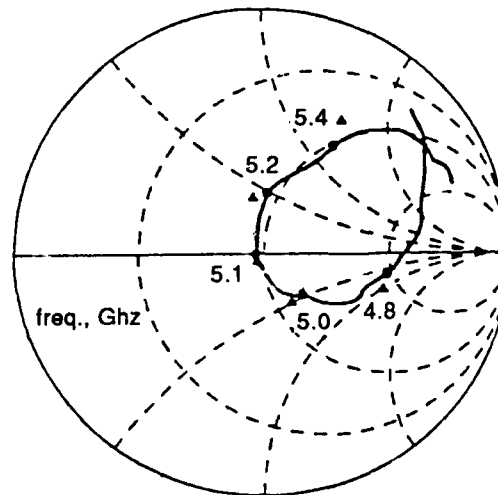


Figure 12. Measured and Computed Input Impedance of Type C Element in Waveguide Simulator

in all three cases. Notice the looped impedance curves of elements A and B due to the double resonances. The second small loop in the impedance curve of Figure 10 between 4.8 and 5.0 GHz is believed to be due to a small amount of leakage from small gaps between the ground plane of the elements and the walls of the waveguide. Ideally, those edges should be soldered together, but for practical purposes, the electrical contact between the element ground plane and the waveguide walls was made by conducting tape.

The impedance characteristics of A and B are very similar, and this can be attributed to the fact that a microstrip feed line behaves very much like a vertical probe feeding the edge of a microstrip patch.¹⁹ Note that there is a phase rotation between the impedance curves of elements A and B due to the different phase references.

Element C has only a single resonance since it has only a single patch and, therefore, has an inherently smaller bandwidth. As can be seen in Figure 12, the predicted and measured results are nearly identical. The close agreement is due to the fact that the type C element does not have any complicated feed current behavior to model, and the single resonance curve is smoothly varying.

As can be seen from Eq. (86), the waveguide simulator cannot replicate the fields of an infinite array at broadside because it would require the wavelength to go to zero. In practice, the simulated incidence angle varies between 20 and 30 degrees, depending upon the frequency.

3.2. 11 X 11 Element Array

Although the waveguide simulator is a very convenient method of simulating an infinite array, the range of scan angles and element spacings that can be simulated are very limited. As a separate check of the analysis, an 11 x 11 array of type A elements was constructed, and the disassembled array is shown in Figure 13. It has been found that five match-loaded elements on all sides of a center element give a reasonably close approximation to an element in an infinite array. More elements will be required to simulate the occurrence of any surface wave resonances.²⁰

The coupling coefficients between the center element and all other elements were measured with the array match-loaded. Using the method described earlier, the mutual coupling coefficients were computed using Eqs. (71) and (82). Figure 14 shows the measured and computed

19. Deshpande, M. and Bailey, M. (1982) Input Impedance of Microstrip Antennas, *IEEE Trans. Antennas and Prop.*, AP-30(No.4):645-650.

20. Amitay, N., Galindo, V., and Wu, C. (1972) *Theory and Analysis of Phased Array Antennas*, Wiley Interscience, New York, p. 366.

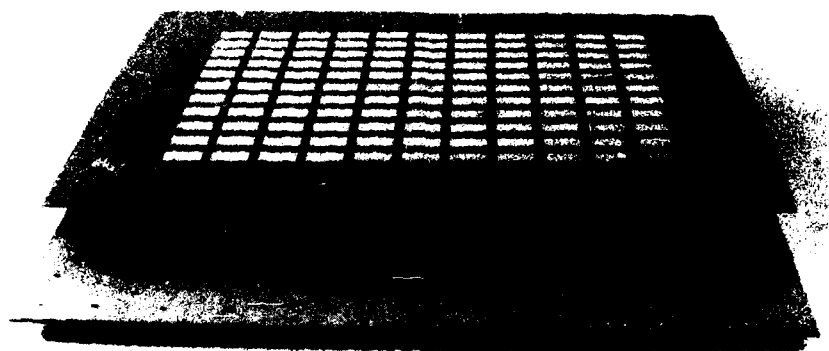


Figure 13. 11 x 11 Array of Type A Elements

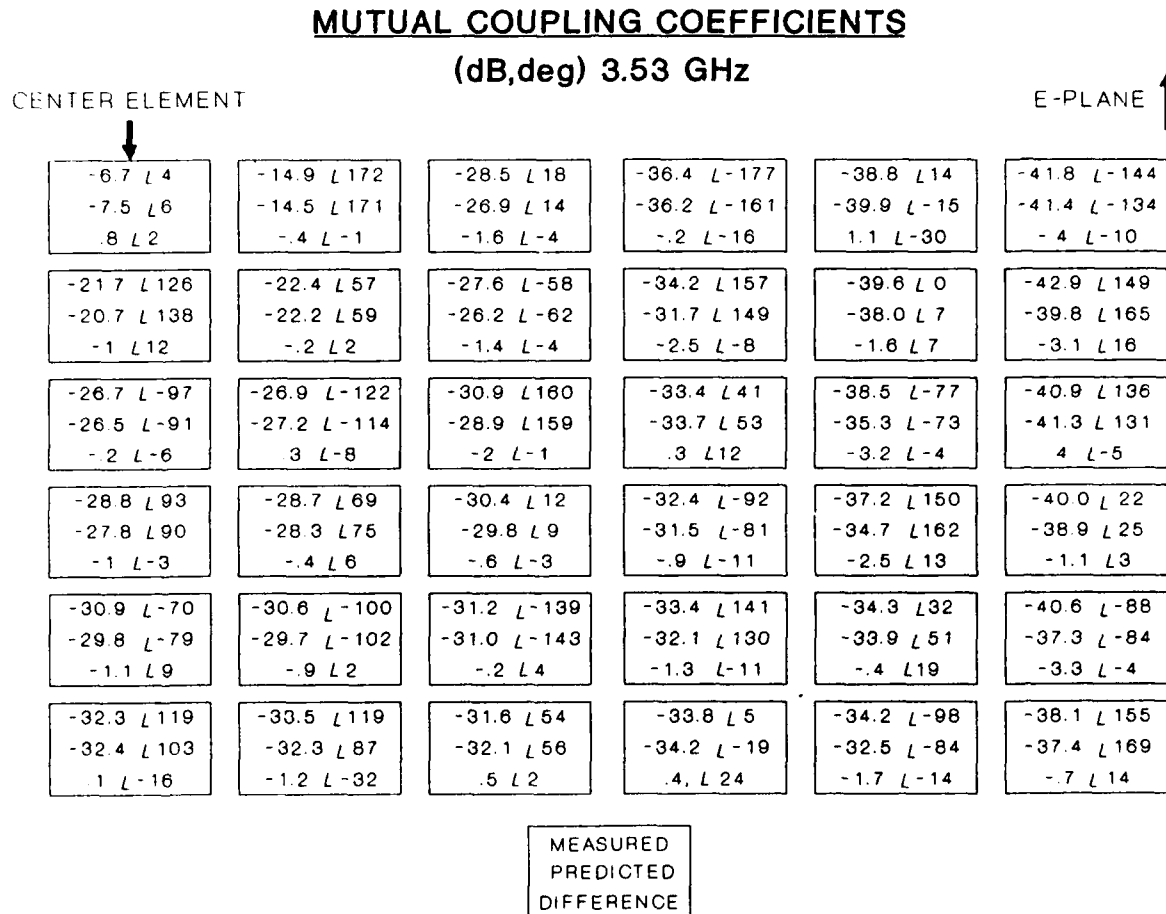


Figure 14. Measured and Computed Mutual Coupling Coefficients for 11 x 11 Array

values for one quadrant of the array at 3.53 GHz. The results agree quite well, and most of the values are closer than 1dB in amplitude and 10 degrees in phase. The larger errors occur for values of coupling less than 35 dB, as would be expected.

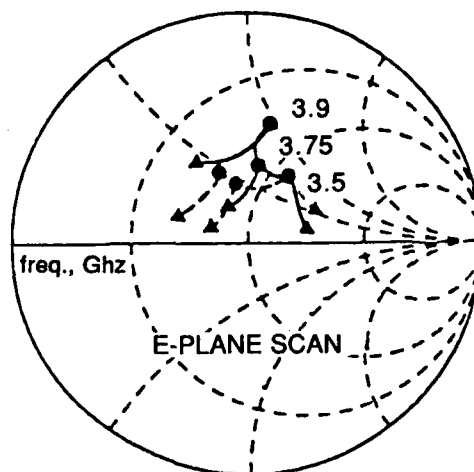
Using the measured mutual coupling coefficients, the active reflection coefficient of the 11 x 11 array was computed by Eq. (80) for E-plane and H-plane scans from 0 degrees to 50 degrees. Figure 15 shows the scanning impedance of the 11 x 11 array compared to the computed infinite array scanning impedance. The measured and computed values agree quite well at the lowest frequency, but begin to depart at the higher frequencies. There appears to be a disagreement between the measured data and the computed data that increases with frequency. The most likely explanation for the difference is that the finite array is not sufficiently large enough to model the infinite array. As mentioned before, a previous study²⁰ has shown that the accurate simulation of infinite array with surface wave effects requires an array larger than 11 x 11.

4. BANDWIDTH LIMITATION STUDY

In the interest of defining the limitations of proximity-coupled patch arrays, a bandwidth study was done for the type A element. To begin with, the bandwidth of an uncovered probe-fed square patch array with one-half wavelength spacing was computed as a function of dielectric thickness. The resonant patch dimension was adjusted so that the input impedance was purely real at broadside, and the bandwidth for a 2:1 VSWR was calculated. The resulting bandwidth for the uncovered patches is shown by the lower solid line in Figure 16. The upper solid line gives the location of the E-plane scan blindness angle as a function of substrate thickness for one-half wavelength array spacing.

Next, a second layer of proximity-coupled patches with the same dielectric constant as the first layer was added, and the upper patch dimension was adjusted for a purely real input impedance. The broadside bandwidth was computed as the upper layer thickness was increased. The dashed curves in Figure 16 show the results for a set of lower layer thicknesses ranging from $0.01\lambda_0$ to $0.05\lambda_0$. As the upper layer thicknesses are increased, it appears that the bandwidths increase asymptotically towards a limit which is approximately 2.5 times the uncovered element bandwidth.

Paschen¹⁹ has tabulated the bandwidth improvement factors obtained by adding lossless resonant sections to a complex load. The values were calculated from the Fano gain-bandwidth integral constraint given by⁸;



$h_1 = .159 \text{ cm}$

$h_2 = .159 \text{ cm}$

$X_1 = .67Y_1 = 2.14 \text{ cm}$

$X_2 = .67Y_2 = 2.30 \text{ cm}$

$\epsilon_1 = 2.33 - j.002$

$\epsilon_2 = 2.33 - j.002$

$a = 3.57 \text{ cm}$

$b = 3.97 \text{ cm}$

--- Predicted

— Measured

● 0° ▲ 50°

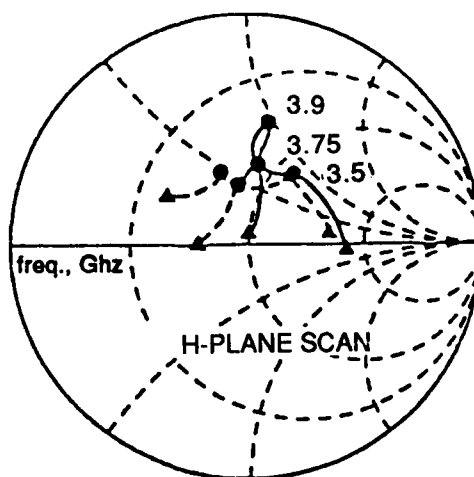


Figure 15. Measured and Computed Scanning Impedance of 11 x 11 Array

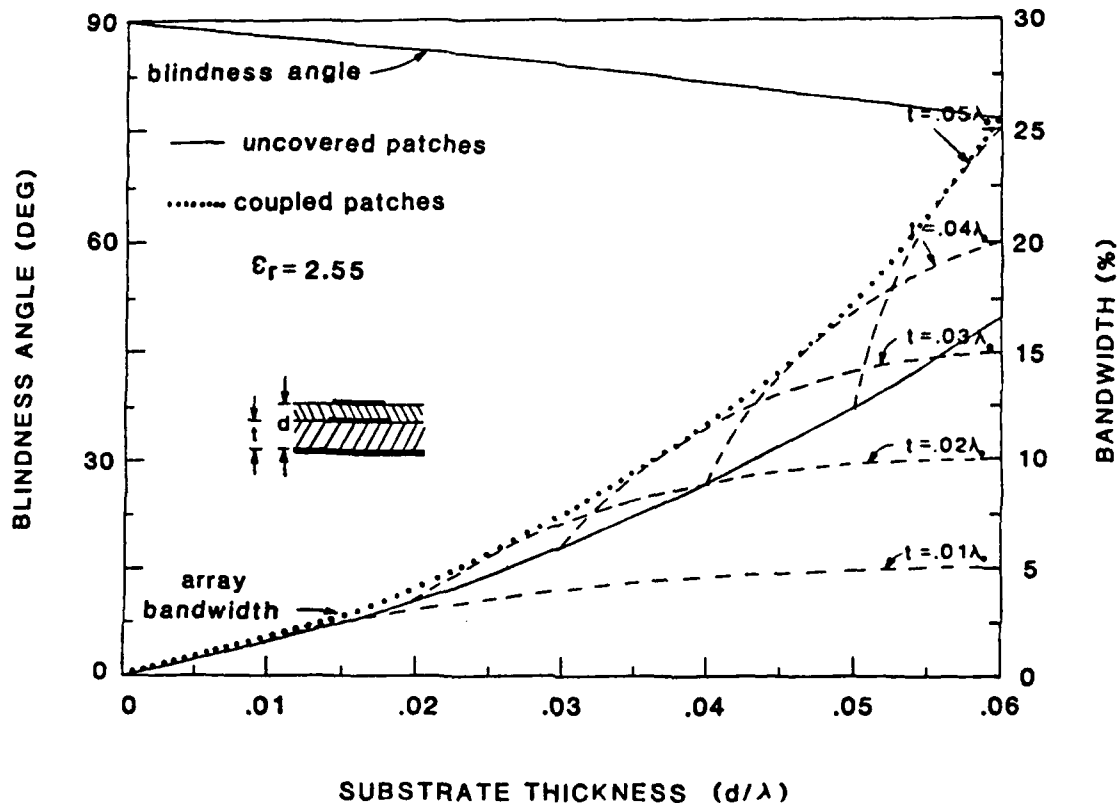


Figure 16. Proximity-Coupled Array Element Bandwidth and Scan Blindness Angle as a Function of Substrate Thickness

$$\int_0^{\infty} \ln |R_n(\omega)| d\omega \leq K \quad (87)$$

where $R_n(\omega)$ is the reflection coefficient of the system with n resonant matching sections, ω is the radian frequency, and K is a constant determined by the impedance of the complex load. This equation implies that there is a physical limit to the frequency bandwidth over which the reflection coefficient of the load can be kept below a certain value. The bandwidth improvement factors for n resonant sections were computed to be²¹;

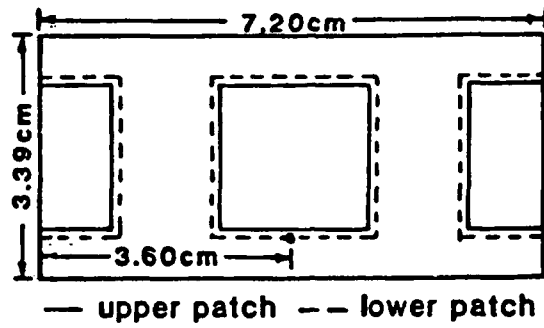
21. Paschen, D. (1983) Broadband Microstrip Matching Techniques, *Allerton Antenna Applications Symposium Digest*, pp.1-20.

<u>number of sections</u>	<u>bandwidth improvement factor</u>
1	2.33
2	2.84
3	3.18
∞	3.86

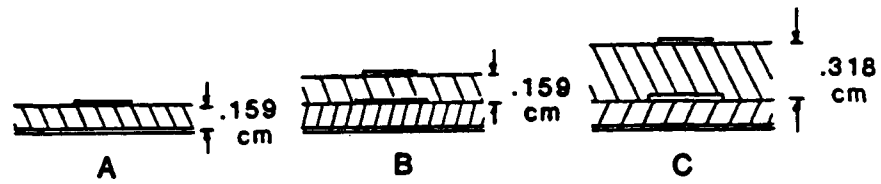
The bandwidth improvement of 2.33 for a single resonant matching section is close to the bandwidth improvement of 2.5 obtained by adding the second layer of resonant patches to the uncovered patch array. If the upper patch behaves like a resonant circuit in parallel with the lower patch, then the bandwidth improvement should be governed by the Fano gain-bandwidth integral constraint. Since the upper patch radiates, it will look like a lossy resonant section, and will, therefore, make the bandwidth improvement slightly larger than the amount predicted by Fano for lossless matching sections. From a practical point of view, this means that the bandwidth is constrained by the uncovered lower patch array.

As a check of these predictions, a set of six measurements were made using the infinite array simulator. Figure 17 shows the different layer combinations for each of the six cases. The upper layer thicknesses were chosen to study the effect on bandwidth of increasing thickness. For case 1, the lower layer thickness was fixed at 0.159 cm. Figure 18 shows the measured and computed input impedance for case 1A, which is an uncovered microstrip element in an infinite array. The bandwidths were computed by normalizing the impedance to the purely real input impedance where the curve crosses the real axis of the Smith chart. Note that the scan angle of the array shifts a small amount with frequency as shown by Eq. (86). Therefore, the bandwidth is computed and measured as the array scans with frequency from 31 degrees at 4.0 GHz to 20 degrees at 6.0 GHz. Figure 19 shows the measured and computed input impedance for case 1B, which has an upper layer thickness of 0.159 cm. There is excellent agreement, and the bandwidth has increased by a factor of 2.2 from case 1A. Figure 20 shows the measured and computed input impedance for case 1C, which has an upper patch layer thickness of 0.318 cm. The results agree very closely, and the bandwidth has increased to 3.0 times the uncovered array bandwidth.

For case 2, the lower layer thickness was fixed at 0.318 cm. Figure 21 shows the measured and computed input impedance of case 2A, which is an uncovered array. Figure 22 shows the measured and computed input impedance for case 2B, which has an upper patch layer thickness of 0.159 cm. The bandwidth has increased considerably to 2.7 times the uncovered array bandwidth. Figure 23 shows the measured and computed input impedance for case 2C, which has an upper patch layer thickness of 0.138 cm. Although the upper layer thickness has been



CASE 1:



CASE 2:

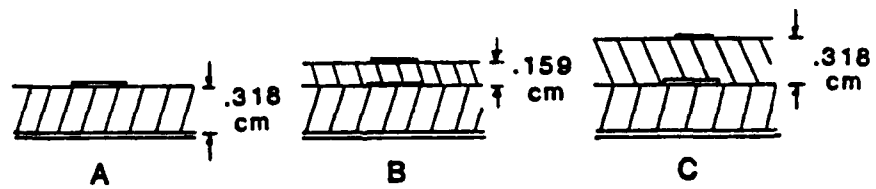
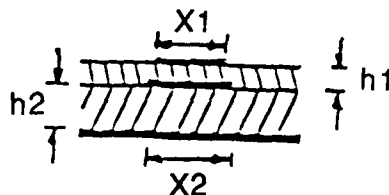


Figure 17. Substrate Combinations for Bandwidth Limitation Study

CASE 1A:

$h_1 = 0 \text{ cm}$
 $h_2 = .159 \text{ cm}$
 $X_1 = Y_1 = 0 \text{ cm}$
 $X_2 = Y_2 = 1.95 \text{ cm}$
 $\epsilon_1 = 2.33 - j.002$
 $\epsilon_2 = 2.33 - j.002$



Measured ●
 (2:1 B.W. 3.9%)

Predicted Δ
 (2:1 B.W. 3.7%)

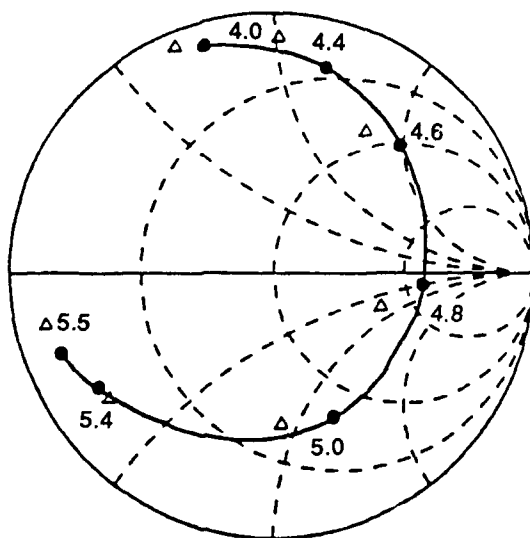
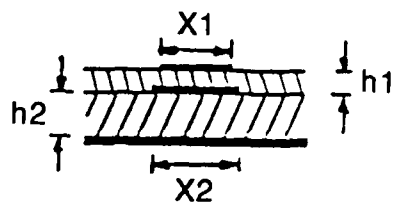


Figure 18. Measured and Computed Input Impedance for Case 1A of Bandwidth Limitation Study

CASE 1B:

$h1 = .159 \text{ cm}$
 $h2 = .159 \text{ cm}$
 $X1 = Y1 = 1.8 \text{ cm}$
 $X2 = Y2 = 1.95 \text{ cm}$
 $\epsilon_1 = 2.33 - j.002$
 $\epsilon_2 = 2.33 - j.002$



Measured ●
 (2:1 B.W. 8.5%)

Predicted △
 (2:1 B.W. 9.0%)

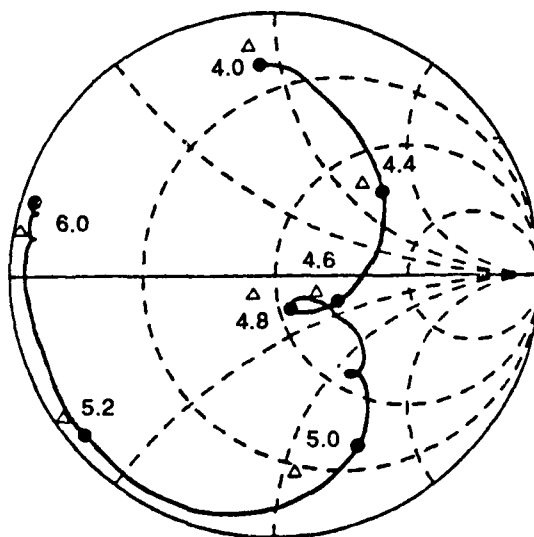


Figure 19. Measured and Computed Input Impedance for Class 1B of Bandwidth Limitation Study

CASE 1C:

$$h1 = .318 \text{ cm}$$

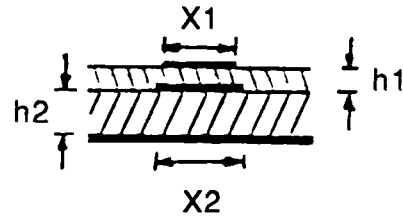
$$h2 = .159 \text{ cm}$$

$$X1 = Y1 = 1.7 \text{ cm}$$

$$X2 = Y2 = 1.95 \text{ cm}$$

$$\epsilon_1 = 2.33 - j.002$$

$$\epsilon_2 = 2.33 - j.002$$



Measured ●
(2:1 B.W. 11.9%)

Predicted △
(2:1 B.W. 11.4%)

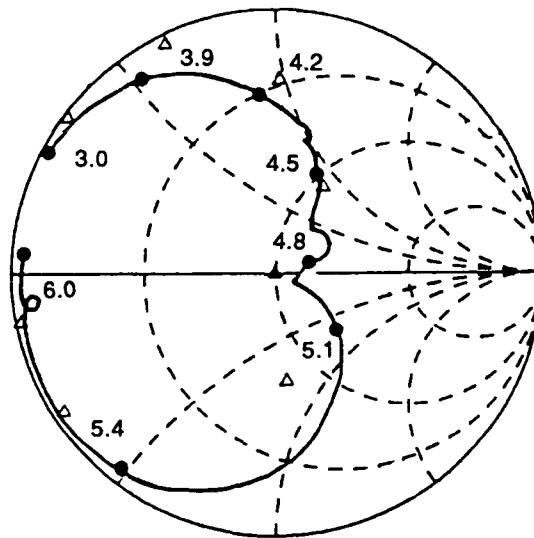
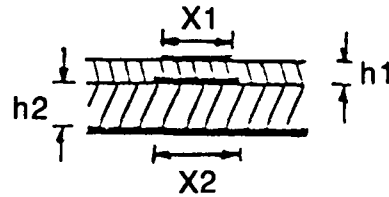


Figure 20. Measured and Computed Input Impedance for Case 1C of Bandwidth Limitation Study

CASE 2A:

$h_1 = 0 \text{ cm}$
 $h_2 = .318 \text{ cm}$
 $X_1 = Y_1 = 0 \text{ cm}$
 $X_2 = Y_2 = 1.95 \text{ cm}$
 $\epsilon_1 = 2.33 - j.002$
 $\epsilon_2 = 2.33 - j.002$



Measured ●
 (2:1 B.W. 6.9%)

Predicted △
 (2:1 B.W. 7.1%)

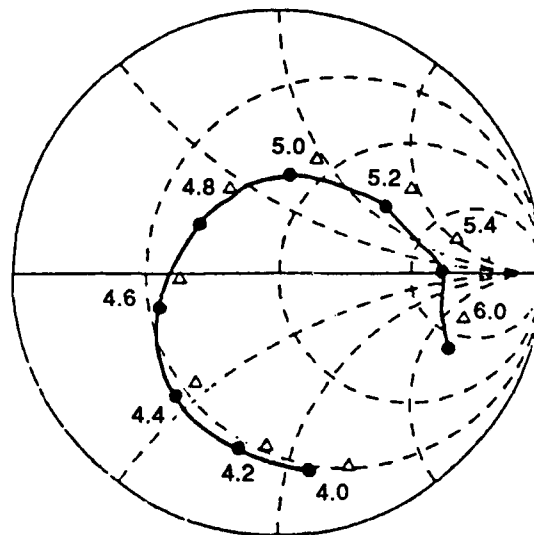
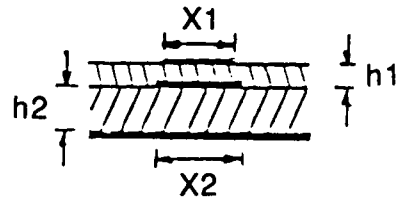


Figure 21. Measured and Computed Input Impedance for Case 2A of Bandwidth Limitation Study

CASE 2B:

$h_1 = .159 \text{ cm}$
 $h_2 = .318 \text{ cm}$
 $X_1 = Y_1 = .1.87 \text{ cm}$
 $X_2 = Y_2 = 1.95 \text{ cm}$
 $\epsilon_1 = 2.33 - j.002$
 $\epsilon_2 = 2.33 - j.002$



Measured ●
 (2:1 B.W. 18.7%)

Predicted △
 (2:1 B.W. 19.2%)

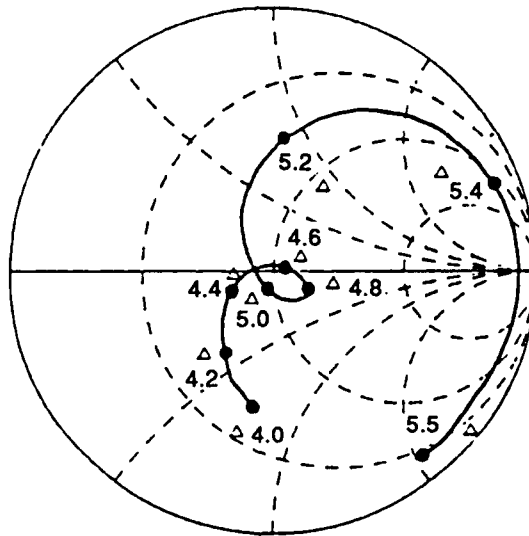
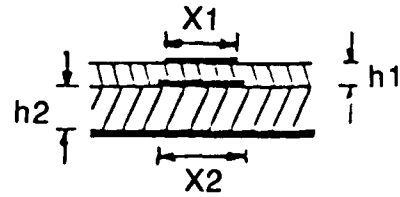


Figure 22. Measured and Computed Input Impedance for Case 2B of Bandwidth Limitation Study

CASE 2C:

$h_1 = .318 \text{ cm}$
 $h_2 = .318 \text{ cm}$
 $X_1 = Y_1 = .1.7 \text{ cm}$
 $X_2 = Y_2 = 1.95 \text{ cm}$
 $\epsilon_1 = 2.33 - j.002$
 $\epsilon_2 = 2.33 - j.002$



Measured ●
(2:1 B.W. 19.5%)

Predicted △
(2:1 B.W. 18.3%)

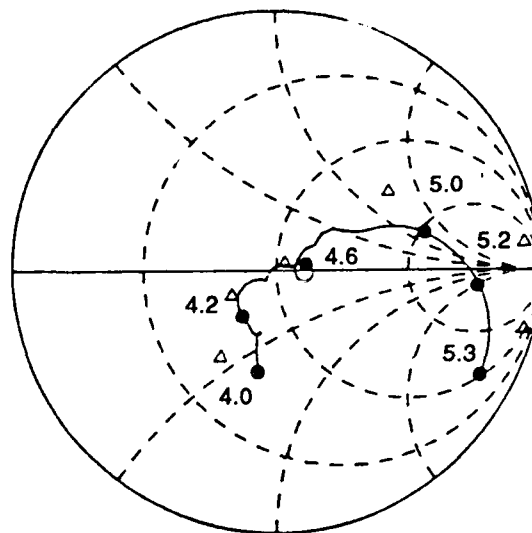


Figure 23. Measured and Computed Input Impedance for Case 2C of Bandwidth Limitation Study

doubled, the bandwidth has only improved a small amount to 2.8 times the uncovered array bandwidth. The results can be summarized as;

<u>case</u>	<u>upper thickness</u>	<u>bandwidth</u>	<u>bandwidth improvement</u>
1A	$0.0\lambda_0$	3.9%	1.0
1B	$0.025\lambda_0$	8.5%	2.2
1C	$0.05\lambda_0$	11.9%	3.0
2A	$0.0\lambda_0$	6.9%	1.0
2B	$0.025\lambda_0$	18.7%	2.7
2C	$0.05\lambda_0$	19.5%	2.8

These results show that, for these parameters, the bandwidth improvement does approach a limit of 2.5 to 3.0 times the uncovered array bandwidth as the upper patch layer thickness is increased. Note that these results represent a trend for the particular dielectric constants and layer thicknesses that were studied. Changes in these parameters may yield better or worse bandwidth improvements, and any variations must be analyzed separately.

5. ARRAY ELEMENT DESIGN STUDY

The bandwidths of the antennas described in the previous section were computed at broadside, and will be reduced by the input impedance variation as the array is scanned off of broadside. To investigate the effects of scanning upon bandwidth, the scanning impedance of several array elements were analyzed.

To begin with, an array element was designed for a broadside bandwidth of 18 percent. Figure 24 shows the input impedance of the element normalized to 50Ω . The small circle at the center of the plot represents the 2:1 VSWR region. The array impedance stays within the 2:1 VSWR circle for scans out to 60 degrees in the E-plane and H-plane at $f=0.91f_0$ and $f=1.05f_0$, but a serious mismatch occurs at the center frequency $f=1.0f_0$ in the H-plane. This example shows that the scanning impedance variation can have a serious effect upon the operating bandwidth of an array, and must be accounted for in the design.

A second array element was designed for scanning bandwidth, and the resulting scan performance is shown in Figure 25. The array has a 14 percent bandwidth at broadside, and can scan over a 50 degree cone with a 10 percent bandwidth. This result was achieved by reducing the H-plane spacing of the elements from $0.5\lambda_0$ to $0.45\lambda_0$, and the aspect ratio of the patches from 1.2 to 1.0. These changes reduced the H-plane scanning impedance variation enough to maintain a match at the center of the band at the expense of overall bandwidth. It has been

$$h1 = .02 \lambda_o$$

$$h2 = .04 \lambda_o$$

$$\epsilon_1 = 2.2$$

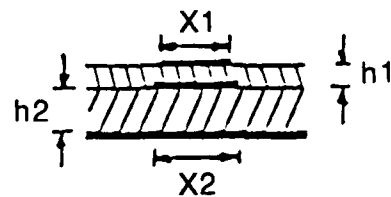
$$\epsilon_2 = 2.2$$

$$X1 = .83 \quad Y1 = .29 \lambda_o$$

$$X2 = .83 \quad Y2 = .31 \lambda_o$$

$$DX = .9 \quad DY = .45 \lambda_o$$

$$Z_{norm} = 50 \Omega$$



$$\bullet \quad \theta = 0^\circ$$

$$\blacksquare \quad \theta = 60^\circ$$

$$- - - \quad \phi = 0^\circ$$

$$- - - \quad \phi = 90^\circ$$

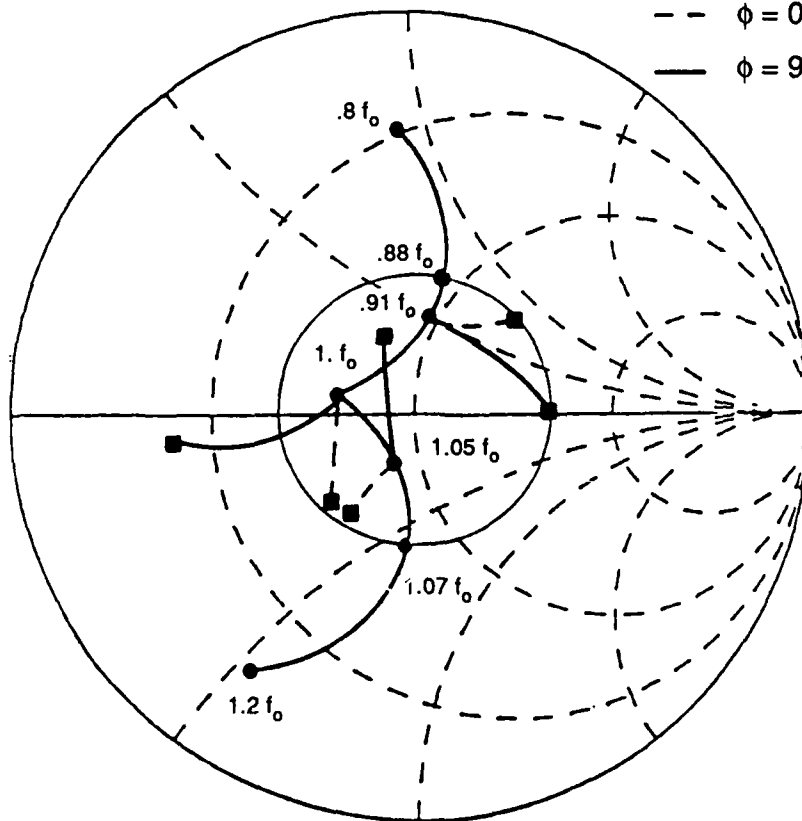


Figure 24. Scanning Impedance of Array Element Optimized for Broadside Bandwidth

$$\begin{aligned}
 h1 &= .02 \lambda_0 \\
 h2 &= .04 \lambda_0 \\
 \epsilon_1 &= 2.2 \\
 \epsilon_2 &= 2.2 \\
 X1 &= Y1 = .29 \lambda_0 \\
 X2 &= Y2 = .31 \lambda_0 \\
 DX &= DY = .45 \lambda_0 \\
 Z_{\text{norm}} &= 50 \Omega
 \end{aligned}$$

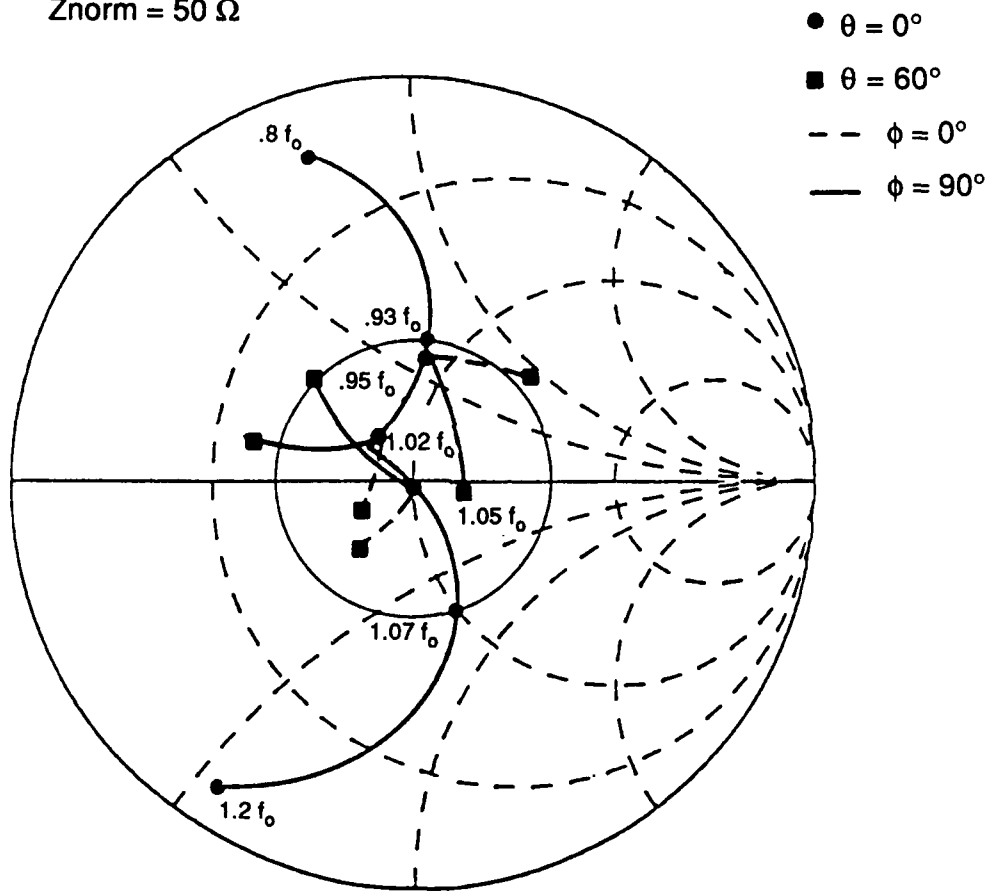
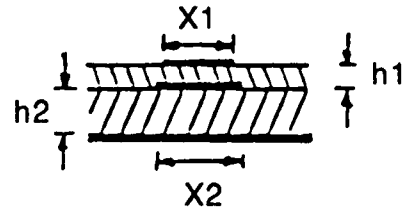


Figure 25. Scanning Impedance of Array Element Optimized for Scanning Bandwidth

suggested²² that a low ϵ_r for the upper layer would further improve the scanning bandwidth.

6. CONCLUSIONS

A full wave analysis was applied to three types of proximity-coupled microstrip array elements. The infinite array spectral dyadic Green's function was used so that all mutual coupling and surface wave effects were included. A method-of-moments was used to solve the electric field integral equation, and three types of expansion modes were used to efficiently model the current distribution on the feed line and patches. By using the approximation that the microstrip feed lines couple only to the unit cell they are feeding, the incident and reflected quasi-TEM fields can be found by integrating over the isolated semi-infinite line with the single element Green's function. This makes it possible to model the field of a traveling wave mode with a source current that extends outside of the unit cell while maintaining the infinite array periodicity.

The scan performance of three proximity-coupled element types was studied. It was found that scan blindness does occur due to surface wave resonances, and a complete E-plane blindness was found for element A, and a large, non-unity reflection was found for elements B and C.

A bandwidth limitation study showed that the bandwidth improvement factor obtained by adding a layer of proximity coupled elements to an uncovered patch array was approximately 2.5. This limit may be related to the theoretical limit for broadband matching of a complex load impedance, as determined by the Fano gain-bandwidth integral constraint. Experimental measurements agree with the results of the bandwidth limitation study.

An array element design study showed that the input impedance of a proximity-coupled array element can vary substantially as a function of scan angle. It was found that the scan performance and bandwidth can be traded off, and an array element was designed with a 10 percent bandwidth over a 50 degree scan cone. The results of this study imply that the design of a proximity-coupled microstrip array with a wide scanning bandwidth must incorporate mutual coupling and surface wave effects.

22. Hansen, R. (1988) in personal communications with the author.

References

1. Yasuo, S., Miyano, N., and Chiba, T. (1983) Expanding the Bandwidth of a Microstrip Antenna, *IEEE AP-S Int. Symp. Digest*, pp 366-369.
2. Sabban, A. (1983) A New Broadband Stacked Two-Layer Microstrip Antenna, *IEEE AP-S Int. Symp. Digest*, pp. 63-66.
3. Chen, H., Tulintseff, A., and Sorbello, R. (1984) A Broadband Two-Layer Microstrip Antenna, *IEEE AP-S Int. Symp. Digest*, pp. 251-254.
4. Cock, R. and Christandoulous, C. (1987) Design of a Two-Layer, Capacitively Coupled, Microstrip Patch Antenna Element for Broadband Applications, *IEEE AP-S Int. Symp. Digest*, pp. 936-939.
5. Pozar, D. and Schaubert, D. (1984) Scan Blindness in Infinite Arrays of Printed Dipoles, *IEEE Trans. Antennas and Prop.*, AP-32:602-610.
6. Pozar, D. and Schaubert, D. (1984) Analysis of an Infinite Array of Rectangular Microstrip Patches with Idealized Probe Feeds, *IEEE Trans. Antennas and Prop.*, AP-32:1101-1107.
7. Pozar, D. (1989) Analysis of an Infinite Phased Array of Aperture Coupled Microstrip Patches, *IEEE Trans. Antennas and Prop.*, AP-37:418-425.
8. Fano, R., (1958) Theoretical Limitations on the Broadband Matching of Arbitrary Impedances, *Journal of the Franklin Institute*, 249:57-84 and 139-154.
9. Pozar, D. (1989) Analysis and Design Considerations for Printed Phased Array Antennas, *Microstrip Antenna Handbook*, J. James and P. Hall, Eds., Peter Peregrinus, London.

10. Jackson, R. and Pozar, D. (1985) Full-Wave Analysis of Microstrip Open-End and Gap Discontinuities, *IEEE Trans. Microwave Theory and Tech.*, MTT-33:1036-1042.
11. Voda, S. and Pozar, D. (1987) A Rigorous Analysis of a Microstrip Line Fed Patch Antenna, *IEEE Trans. Antennas and Prop.*, AP-35:1343-1350.
12. Chew, W. and Kong, J. (1981) Analysis of a Circular Microstrip Disk Antenna with a Thick Dielectric Substrate, *IEEE Trans. Antennas and Prop.*, AP-29:68-76.
13. Liu, C., Hessel, A., and Shmoys, J. (1985) Performance of Probe-Fed Microstrip-Patch Element Phased Arrays, *Phased Arrays 1985 Symposium Digest*, pp. 157-176.
14. Aberle, J. and Pozar, D. (1989) Analysis of Infinite Arrays of Probe-Fed Rectangular Microstrip Patches Using a Rigorous Feed Model, *IEE Proceedings*, 136, Pt. H, No. 2.
15. Newman, E. and Forrai, D. (1987) Scattering from a Microstrip Patch, *IEEE Trans. Antennas and Prop.*, AP-35.
16. Rana, I. and Alexopoulos, N. (1981) Current Distribution and Input Impedance of Printed Dipoles, *IEEE Trans. Antennas and Prop.*, AP-29:99-105.
17. Alexopoulos, N. and Rana, I. (1981) Mutual Impedance Computation Between Printed Dipoles, *IEEE Trans. Antennas and Prop.*, AP-29(No. 1):106-111.
18. Hansen, R., (ed.) (1966) *Microwave Scanning Antennas*, Vol.II, *Array Theory and Practice*, Academic Press, New York.
19. Deshpande, M. and Bailey, M. (1982) Input Impedance of Microstrip Antennas, *IEEE Trans. Antennas and Prop.*, AP-30(No.4):645-650.
20. Amitay, N., Galindo, V., and Wu, C. (1972) *Theory and Analysis of Phased Array Antennas*, Wiley Interscience, New York, p. 366.
21. Paschen, D. (1983) Broadband Microstrip Matching Techniques, *Allerton Antenna Applications Symposium Digest*, pp.1-20.
22. Hansen, R. (1988) in personal communications with the author.

Appendix: Spectral Dyadic Green's Function

The spectral dyadic Green's functions that are needed for the analysis are given by;

$$\begin{aligned}
 Q_{xx1}[z=h_2] = & \frac{jZ_0}{k_0} \frac{\sin k_2' h_2}{\epsilon_2 T_e} \left\{ \left(\epsilon_2 k_0^2 - k_x^2 \right) \left[k_1' \cos k_1' h_1 + j k_0' \sin k_1' h_1 \right] \right. \\
 & \frac{j k_2' k_x^2 \sin k_2' h_2}{T_m} \left[\left(\frac{\epsilon_2}{\epsilon_1} - 1 \right) \left[k_1' \cos k_1' h_1 + j k_0' \sin k_1' h_1 \right] \cdot \right. \\
 & \left. \left. \left[k_1' \cos k_1' h_1 + j \epsilon_1 k_0' \sin k_1' h_1 \right] + k_1'^2 \left[\epsilon_2 \frac{\epsilon_2}{\epsilon_1} \right] \right] \right\}
 \end{aligned} \tag{88}$$

$$\begin{aligned}
 Q_{xx1}[z=h_1+h_2] = Q_{xx2}[z=h_2] = & \frac{jZ_0}{k_0} \frac{k_1' \sin k_2' h}{\epsilon_1 T_e} \left\{ \left(\epsilon_2 k_0^2 - k_x^2 \right) + \frac{k_x^2}{T_m} \left[\left(\frac{\epsilon_2}{\epsilon_1} - 1 \right) \left[\epsilon_1 k_0' \cos k_2' h_2 \right] \cdot \right. \right. \\
 & \left. \left. \left[k_1' \cos k_1' h_1 + j k_0' \sin k_1' h_1 \right] - j k_1' \left[\epsilon_1 - 1 \right] \cdot \right. \right\}
 \end{aligned}$$

$$\left[\frac{\epsilon_2}{\epsilon_1} k_1' \cos k_1' h_1 \cos k_2' h_2 + k_2' \sin k_1' h_1 \sin k_2' h_2 \right] \quad (89)$$

$$\begin{aligned} Q_{yx1}[z=h_2] &= Q_{xy1}[z=h_1] = \\ &= \frac{jZ_0}{k_0} \frac{-k_x k_y \sin k_2' h_2}{\epsilon_2 T_m T_e} \left\{ \left[k_1' \cos k_1' h_1 + jk_0' \sin k_1' h_1 \right] T_m \right. \\ &+ jk_2' \sin k_2' h_2 \left[\left(\frac{\epsilon_2}{\epsilon_1} - 1 \right) \left[k_1' \cos k_1' h_1 + j\epsilon_1 k_0' \sin k_1' h_1 \right] \cdot \right. \\ &\left. \left. \left[k_1' \cos k_1' h_1 + jk_0' \sin k_1' h_1 \right] + k_1'^2 \left[\epsilon_2 \frac{\epsilon_2}{\epsilon_1} \right] \right] \right\} \quad (90) \end{aligned}$$

$$\begin{aligned} Q_{yx1}[z=h_1+h_2] &= Q_{xy1}[z=h_1+h_2] = Q_{yx2}[z=h_2] = Q_{xy2}[z=h_2] = \\ &= \frac{jZ_0}{k_0} \frac{-k_x k_y k_1' \sin k_2' h_2}{T_e} \left\{ 1 - \frac{k_0'}{T_m} \left[\frac{\epsilon_2}{\epsilon_1} - 1 \right] \left[\cos k_2' h_2 \right] \cdot \right. \\ &\left. \left[k_1' \cos k_1' h_1 + jk_0' \sin k_1' h_1 \right] + \left[\epsilon_1 - 1 \right] \cdot \right. \\ &\left. \left. \left[\frac{\epsilon_2}{\epsilon_1} k_1' \cos k_1' h_1 \cos k_2' h_2 + k_2' \sin k_1' h_1 \sin k_2' h_2 \right] \right\} \quad (91) \end{aligned}$$

$$\begin{aligned} Q_{yy1}[z=h_2] &= \\ &= \frac{jZ_0}{k_0} \frac{\sin k_2' h_2}{\epsilon_2 T_e} \left\{ \left[\epsilon_2 k_0'^2 - k_y'^2 \right] \left[k_1' \cos k_1' h_1 + jk_0' \sin k_1' h_1 \right] \right. \\ &+ \frac{jk_2' k_y'^2 \sin k_2' h_2}{T_m} \left[\left(\frac{\epsilon_2}{\epsilon_1} - 1 \right) \left[k_1' \cos k_1' h_1 + jk_0' \sin k_1' h_1 \right] \cdot \right. \\ &\left. \left. \left[k_1' \cos k_1' h_1 + j\epsilon_1 k_0' \sin k_1' h_1 \right] + k_1'^2 \left[\epsilon_2 \frac{\epsilon_2}{\epsilon_1} \right] \right] \right\} \quad (92) \end{aligned}$$

$$\begin{aligned}
Q_{yy1}[z=h_1+h_2] &= Q_{yy2}[z=h_2] = \\
&\frac{jZ_0}{k_0} \frac{k_1' \sin k_2' h_2}{\epsilon_1 T_e} \left\{ \left(\epsilon_2 k_0^2 - k_y^2 \right) + \frac{k_y^2}{T_m} \left[\left(\frac{\epsilon_2}{\epsilon_1} - 1 \right) \left(\epsilon_1 k_0' \cos k_2' h_2 \right) \cdot \right. \right. \\
&\left. \left. \left(k_1' \cos k_1' h_1 + j k_0' \sin k_1' h_1 \right) - j k_1' \left(\epsilon_1 - 1 \right) \cdot \right. \right. \\
&\left. \left. \left(\frac{\epsilon_2}{\epsilon_1} k_1' \cos k_1' h_1 \cos k_2' h_2 + k_2' \sin k_1' h_1 \sin k_2' h_2 \right) \right\} \right. \quad (93)
\end{aligned}$$

$$\begin{aligned}
Q_{xx2}[z=h_1+h_2] &= \\
&\frac{jZ_0}{k_0} \frac{1}{\epsilon_1 T_e} \left\{ \left(\epsilon_1 k_0^2 - k_x^2 \right) \left[k_1' \cos k_1' h_1 \sin k_2' h_2 + k_2' \sin k_1' h_1 \cos k_2' h_2 \right] \right. \\
&+ \frac{k_1' k_x^2}{T_m} \left[\left(\epsilon_2 - \epsilon_1 \right) \left(k_0' k_1' \cos k_2' h_2 \sin k_2' h_2 \right) - \right. \\
&j \left(\epsilon_1 - 1 \right) \left(k_1' \cos k_1' h_1 \sin k_2' h_2 + k_2' \sin k_1' h_1 \cos k_2' h_2 \right) \cdot \\
&\left. \left. \left(\frac{\epsilon_2}{\epsilon_1} k_1' \cos k_2' h_2 \sin k_1' h_1 + k_2' \sin k_2' h_2 \cos k_1' h_1 \right) \right] \right\} \quad (94)
\end{aligned}$$

$$\begin{aligned}
Q_{yx2}[z=h_1+h_2] &= Q_{xy2}[z=h_1+h_2] = \\
&\frac{jZ_0}{k_0} \frac{-k_x k_y}{\epsilon_1 T_e} \left\{ \left[k_1' \cos k_1' h_1 \sin k_2' h_2 + k_2' \sin k_1' h_1 \cos k_2' h_2 \right] \right. \\
&- \frac{k_1'}{T_m} \left[\left(\frac{\epsilon_2}{\epsilon_1} - 1 \right) \left(\epsilon_1 k_0' k_1' \cos k_2' h_2 \sin k_2' h_2 \right) - \right. \\
&j \left(\epsilon_1 - 1 \right) \left(k_1' \cos k_1' h_1 \sin k_2' h_2 + k_2' \sin k_1' h_1 \cos k_2' h_2 \right) \cdot \\
&\left. \left. \left(\frac{\epsilon_2}{\epsilon_1} k_1' \cos k_2' h_2 \sin k_1' h_1 + k_2' \sin k_2' h_2 \cos k_1' h_1 \right) \right] \right\} \quad (95)
\end{aligned}$$

$$\begin{aligned}
Q_{yy2}[z=h_1+h_2] = & \\
& \frac{jZ_0}{k_0} \frac{1}{\epsilon_1 T_e} \left\{ \left(\epsilon_1 k_0^2 - k_y^2 \right) \left[k_1' \cos k_1' h_1 \sin k_2' h_2 + k_2' \sin k_1' h_1 \cos k_2' h_2 \right] \right. \\
& + \frac{k_1' k_y^2}{T_m} \left[\left(\epsilon_2 - \epsilon_1 \right) \left[k_0' k_1' \cos k_2' h_2 \sin k_2' h_2 \right] - \right. \\
& j \left(\epsilon_1 - 1 \right) \left[k_1' \cos k_1' h_1 \sin k_2' h_2 + k_2' \sin k_1' h_1 \cos k_2' h_2 \right] \cdot \\
& \left. \left. \cdot \left[-\frac{\epsilon_2}{\epsilon_1} k_1' \cos k_2' h_2 \sin k_1' h_1 + k_2' \sin k_2' h_2 \cos k_1' h_1 \right] \right] \right\} \quad (96)
\end{aligned}$$

$$\begin{aligned}
Q_{xz1}[z=h_2] = Q_{zx1}[z=h_2] = & \\
& \frac{jZ_0}{k_0} \frac{2 \sin k_2' h_2}{\epsilon_1 k_2'} \left\{ \left(\epsilon_1 k_0^2 - k_2^2 \right) \left[\frac{k_x \sin k_2' h_2}{\epsilon_2 T_m T_e} \right] \left[\left(\frac{\epsilon_2}{\epsilon_1} - 1 \right) \cdot \right. \right. \\
& \left[k_1' \cos k_1' h_1 + j k_0' \sin k_1' h_1 \right] \left[k_1' \cos k_1' h_1 + j \epsilon_1 k_0' \sin k_1' h_1 \right] \\
& \left. \left. + k_1'^2 \left(\epsilon_2 - \frac{\epsilon_2}{\epsilon_1} \right) \right] - \frac{k_2' k_x}{2j T_e} \left[k_1' \cos k_1' h_1 + j k_0' \sin k_1' h_1 \right] \right\} \quad (97)
\end{aligned}$$

$$\begin{aligned}
Q_{yz1}[z=h_2] = Q_{zy1}[z=h_2] = & \\
& \frac{jZ_0}{k_0} \frac{2 \sin k_2' h_2}{\epsilon_1 k_2'} \left\{ \left(\epsilon_1 k_0^2 - k_2^2 \right) \left[\frac{k_y \sin k_2' h_2}{\epsilon_2 T_m T_e} \right] \left[\left(\frac{\epsilon_2}{\epsilon_1} - 1 \right) \cdot \right. \right. \\
& \left[k_1' \cos k_1' h_1 + j k_0' \sin k_1' h_1 \right] \left[k_1' \cos k_1' h_1 + j \epsilon_1 k_0' \sin k_1' h_1 \right] \\
& \left. \left. + k_1'^2 \left(\epsilon_2 - \frac{\epsilon_2}{\epsilon_1} \right) \right] - \frac{k_2' k_y}{2j T_e} \left[k_1' \cos k_1' h_1 + j k_0' \sin k_1' h_1 \right] \right\} \quad (98)
\end{aligned}$$

$$\begin{aligned}
Q_{xz1}[z=h_1+h_2] &= Q_{xz2}[z=h_2] = \\
&\frac{jZ_0}{k_0} \frac{2 \sin k_2' h}{\epsilon_1 k_2'} \left\{ \left[\epsilon_2 k_0^2 - k_2'^2 \right] \left[\frac{k_x}{2T_m T_e} \right] \left[\left(\frac{\epsilon_2}{\epsilon_1} - 1 \right) \cdot \right. \right. \\
&\left. \left[k_1' \cos k_1' h_1 + j\epsilon_1 k_0' \sin k_1' h_1 \right] \left[k_1' \sin k_2' h_2 \right] + k_1' \left[\epsilon_2 - \epsilon_1 \right] \cdot \right. \\
&\left. \left. \left[k_1' \cos k_1' h_1 \sin k_2' h_2 + k_2' \sin k_1' h_1 \cos k_2' h_2 \right] \right] - \frac{k_1' k_2' k_x}{2j T_e} \right\} \quad (99)
\end{aligned}$$

$$\begin{aligned}
Q_{yz1}[z=h_1+h_2] &= Q_{yz2}[z=h_2] = \\
&\frac{jZ_0}{k_0} \frac{2 \sin k_2' h}{\epsilon_1 k_2'} \left\{ \left[\epsilon_2 k_0^2 - k_2'^2 \right] \left[\frac{k_y}{2T_m T_e} \right] \left[\left(\frac{\epsilon_2}{\epsilon_1} - 1 \right) \cdot \right. \right. \\
&\left. \left[k_1' \cos k_1' h_1 + j\epsilon_1 k_0' \sin k_1' h_1 \right] \left[k_1' \sin k_2' h_2 \right] + k_1' \left[\epsilon_2 - \epsilon_1 \right] \cdot \right. \\
&\left. \left. \left[k_1' \cos k_1' h_1 \sin k_2' h_2 + k_2' \sin k_1' h_1 \cos k_2' h_2 \right] \right] - \frac{k_1' k_2' k_y}{2j T_e} \right\} \quad (100)
\end{aligned}$$

where

$$Q_{pqr} = \begin{cases} p = \text{field direction (x, y, or z)} \\ q = \text{source direction (x, y, or z)} \\ r = 1 \text{ for source at } z=h_1+h_2 \\ r = 2 \text{ for source at } z=h_2 \end{cases} \quad (101)$$

$$\begin{aligned}
T_e &= k_2' \cos k_2' h_2 \left[k_1' \cos k_1' h_1 + jk_0' \sin k_1' h_1 \right] \\
&+ jk_1' \sin k_2' h_2 \left[k_0' \cos k_1' h_1 + jk_1' \sin k_1' h_1 \right] \quad (102)
\end{aligned}$$

$$\begin{aligned}
T_m &= \frac{\epsilon_2}{\epsilon_1} k_1' \cos k_2' h_2 \left[\epsilon_1 k_0' \cos k_1' h_1 + jk_1' \sin k_1' h_1 \right] \\
&+ jk_2' \sin k_2' h_2 \left[k_1' \cos k_1' h_1 + j\epsilon_2 k_0' \sin k_1' h_1 \right] \quad (103)
\end{aligned}$$

$$k_0'^2 = k_0^2 - \beta^2 \quad (104)$$

$$k_1'^2 = \epsilon_1 k_0^2 - \beta^2 \quad (105)$$

$$k_2'^2 = \epsilon_2 k_0^2 - \beta^2 \quad (106)$$

$$\beta^2 = k_x^2 + k_y^2 \quad (107)$$

$$Z_0 = \sqrt{\mu_0 / \epsilon_0} \quad (108)$$

$$k_0 = \frac{2\pi}{\lambda_0} \quad (109)$$

The z-directed components were obtained by integrating over the z-directed probe of constant current and height h_2 .



MISSION of Rome Air Development Center

RADC plans and executes research, development, test and selected acquisition programs in support of Command, Control, Communications and Intelligence (C³I) activities. Technical and engineering support within areas of competence is provided to ESD Program Offices (POs) and other ESD elements to perform effective acquisition of C³I systems. The areas of technical competence include communications, command and control, battle management, information processing, surveillance sensors, intelligence data collection and handling, solid state sciences, electromagnetics, and propagation, and electronic maintainability, and compatibility.